Summer 8-7-2020

Forecasting the Development of a Natural Levee Breach and Subsequent Sediment Distribution at Mardi Gras Pass, Louisiana

Joshua Hansen
University of New Orleans, jhansen@uno.edu

Forecasting the Development of a Natural Levee Breach and Subsequent Sediment Distribution at Mardi Gras Pass, Louisiana

A Thesis

Submitted to the Graduate Faculty of the
University of New Orleans
in partial fulfillment of the
requirements for the degree of

Master of Science
in
Earth and Environmental Science
Coastal Sciences

by

Joshua Hansen

B.S. Towson University, 2012

August, 2020

Acknowledgments

A special thanks to:

My parents, Scott and Esperanza Hansen, and my partner, Melissa Ciampo, for their unflagging support of my endeavors. Keller Black, who was nice enough to lend me his desktop computer to aid in my research.

The Lake Pontchartrain Basin Foundation for its partial funding of field data collection.

And for their efforts in field and technical support:

Ben Beasley
Mike Brown
Tara Yocum
Sakib Mohuiddin

All of whom worked on behalf of the Department of Earth and Environmental Sciences, University of New Orleans, and the Pontchartrain Institute for Environmental Sciences, University of New Orleans, New Orleans LA.

Table of Contents

List of Figures

List of Tables

List of Equations

Nomenclature and Abbreviations

ADCP ..... Acoustic Doppler Current Profiler
BLC ..... Back Levee Canal
BLC_JB SPLIT ..... Back Level Canal and John Bayou Junction
CoNED ..... Coastal National Elevation Database
E ..... Erosion Rate
D ..... Deposition Rate
DGPS ..... Differential GPS
FB ..... Fucich Bayou
GNSS ..... Global Navigation Satellite Systems
GPS ..... Global Positioning System
LISST ..... Laser In-Situ Scattering and Transmissometry
LGB ..... Lower Grand Bayou
JB ..... John Bayou
MGP ..... Mardi Gras Pass
MR ..... Mississippi River
MRD ..... Mississippi River Delta
NGO ..... Non-Government Organization
NoMGP_BLC ..... North of Mardi Gras Pass on the BLC
RBR ..... Richard Brancker Research
RTK ..... Real-Time Kinematic
SoMGP_BLC ..... South of Mardi Gras Pass on the BLC
SSC ..... Suspended Sediment Concentration
SST ..... Suspended Sediment Transport
TSS ..... Total Suspended Solids

Abstract

In 2012, a breach in a natural levee occurred on the Mississippi River near the Bohemian Spillway, forming a new distributary named Mardi Gras Pass. Since its genesis, scientists from local universities and NGOs have been regularly performing bathymetric and bank surveys to track the channel's expansion, as well as discharge surveys throughout the receiving basin. This study developed and implemented a hindcast simulation based on this wealth of data utilizing the morpho- and hydrodynamic model, Delft3D. This model was then used to create a 20-year forecast and a 1-year simulation without tidal and subtidal forces. The results demonstrated that tides were a major influence on water levels, discharge rates, and sedimentation patterns. The forecast suggested that an avulsion is not likely in the near future. However, channel reorganizing within the floodplain occurred as preferential flow and deposition trends developed based on the physical parameters determined by the hindcast.

Keywords: Avulsion, Breach, Levee, Natural, Sediment Diversion, Crevasse Splay, floodplain, Mardi Gras Pass, Mississippi River, Sea Level Rise

Introduction

Deltas have and continue to be one of the most important landforms with regard to human civilization. Being among the most bioproductive and biodiverse landforms, deltas have been some of the most heavily populated regions. In addition, their high bioproductivity, they are abundant in hydrocarbon resources. The inherent nature of deltas, with its interconnected webs of river channels and bays with direct access to the ocean, have proven favorable for the development of well-known port cities such as Amsterdam, Bangkok, and New Orleans (Chamberlain, 2018)

Formed at the intersection of rivers and the open sea, deltas are the location of major depocenters. Sediments providenced by a river's drainage region is deposited to form a span of floodplains and marshes. Land growth can occur in several ways, depending on a multitude of factors. For example, coarser sediments are deposited at the river's mouth, allowing progradation to occur. Aggradation occurs when annual flooding overtops the river banks and delivers finer sediments to the floodplain, allowing it to increase in elevation. Therefore, deltas are considered one of the most complex geologic systems (Chamberlain, 2018).

Left to nature, rivers will meander, tearing through old lands and creating new pathways. Avulsions occur during episodes known as delta switching (Chamberlain, 2018). These sudden and consequential movements happen around a divergence point when a flood event of a sufficient magnitude happens along a river that is near or at its "avulsion threshold." The "avulsion threshold" is a dynamic set of conditions that are defined by the ever-changing channel instability. Given this definition, it is implied that the largest flood won't necessarily equate as a trigger for avulsions in a given river. However, given the right conditions, a small flood could activate an avulsion if the given river is near its "avulsion threshold." Crevasse splaying is a common mechanism of avulsion, which occurs via the gradual breaching through the banks and the creation of a new channel over time. Another common process is channel reoccupation, where pre-existing channels within the vicinity are occupied by new channels (Sinha, 2008).

Depending on a litany of processes, levee breaches may persist for centuries, developing into a crevasse splay. Conversely, they may also close quickly or undergo avulsion (Fisk, 1952; Smith, Cross, Dufficy, & Clough, 1989). However, the conditions for avulsion and crevasse splay formation are still poorly understood. This knowledge gap must be bridged, because these processes are excellent land building systems, and serve as a natural analog to aid the planning and design of sediment diversions being developed by the Coastal Protection and Restoration Authority (CPRA, 2017; Gagliano & Van Beek, 1975) in the Mississippi River Delta (MRD).

Avulsions are of concern to coastal management officials because any immediate development will be detrimental to existing infrastructure and industries that rely on the river's current placement for navigation and freshwater delivery. The high density of human population within deltas, and nearby rivers, necessitates that avulsions do not occur. In 2008, an avulsion of the Kosi River in eastern India had been considered one of the greatest avulsions in recent history. This event recorded an eastward jump of ~120 km, waterlogging the impacted area for 4 months, and affecting more than 30 million people with over 200 casualties (Sinha, 2008). Disasters like these necessitate more research to be done to study channel evolution of nascent levee breaches to develop a framework for its development into a main distributary.

Background

In 2011, a historic flood occurred on the Mississippi River (MR) due to extreme rains and snowmelt in the watershed. During this event, the Bohemia Spillway in Louisiana was overtopped, causing extensive flooding. The maximum flow at the spillway during the 2011 flood reached to between 30,000 and 50,000 $ft^3\ s^{-1}$. As a result, two breaches developed in the river adjacent to Bohemia Road. One formed near the Diversion Control, and the other further south, near the gas field (Figure 2) (Lopez, et al., 2013).

Figure 1.
Overview of the study area.

The breach adjacent to the Diversion Canal proceeded to expand as the waters rescinded due to headward erosion towards the river cutting through a sand bar parallel to the Mississippi River's edge (Figure 3). During a later high-water event in 2012, additional headward erosion continued to eventually create a cut through to the Mississippi River, forming a new distributary named Mardi Gras Pass (MGP) (Figure 4) (Lopez et al., 2013).

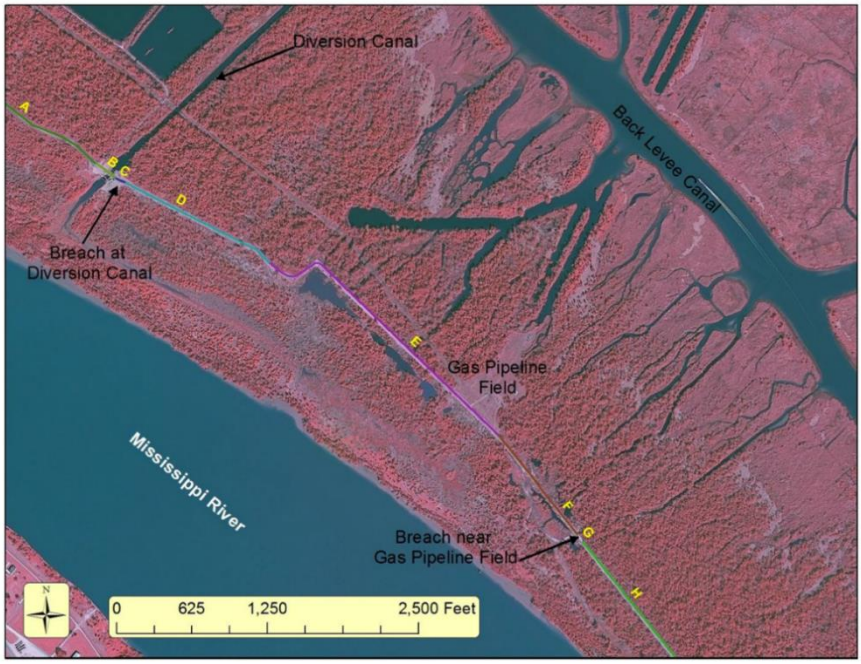

Figure 2.
Location of breaches formed during the 2011 Mississippi River Flood (Lopez et al, 2013).

Figure 3.
The extent of the breach and headward erosion in 2011 (Lopez et al., 2013).

Figure 4.
The newly created distributary Mardi Gras Pass (Lopez et al., 2013)

Since its genesis, scientists from local universities and NGOs have been regularly performing bathymetric and bank surveys to track the channel's expansion. In addition, Acoustic Doppler Current Profiler surveys were conducted to accurately measure the discharge flowing through Mardi Gras Pass as it evolves (Lopez et al., 2013). Between 2012 and 2016, the channel's average width more than doubled from ~81 ft (25 m) to ~184 ft (56 m), respectively. As of November 2017, the width has increased to ~200 ft (61 m) (Boyd et al., 2012; Cretini et al., 2016; Songy et al., 2018). From 2012 to 2017, the average cross-sectional area has increased from 705 ft^2 (65 m^2) to 4,924 ft^2 (457 m^2), respectively (Boyd et al. 2012, Songy et al. 2018). Since the breach, high annual flows during flood season have consistently created conditions favoring erosion of the channel bed, modifying the channel depth and shape. Contrastingly, the bed remains relatively unchanged during low flow seasons (non-eroding), and often even favors deposition towards the receiving basin (Henkel et al., 2018).

There is a 10 – 15 % tidal modulation of the flow distribution at MGP and Back Levee Canal (BLC) from neap to spring conditions, and approximately 8 – 13% from falling to rising tides (Figures 5 & 6) (Georgiou & Yocum, 2018). Spring-neap variation and rising or falling tides exhibit a 3 – 5% change upon the flow distribution between John Bayou and Fucich Bayou, implying that tides have a lesser effect at modulating the long-term average of 50/50 (Figures 5 & 6) (Georgiou & Yocum, 2018). To date, all evidence has shown that there has been a positive increase in channel dimensions and discharge for the pass. The rate of enlargement is an indication of increasing stream capture of the Mississippi River flow.

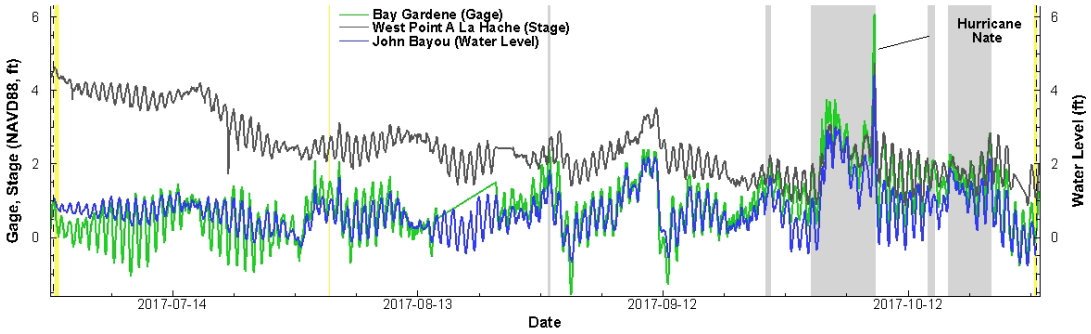

Figure 5.
(Blue) Measured water level anomaly in John Bayou. (Black) Mississippi River stage (ft) at West Pointe A La Hache. (Green) Tide gage measurements were taken during the deployment period in Bay Gardene. (Yellow) Synoptic ADCP surveys. (Gray) Times of flow reversals (Georgiou & Yocum, 2018).

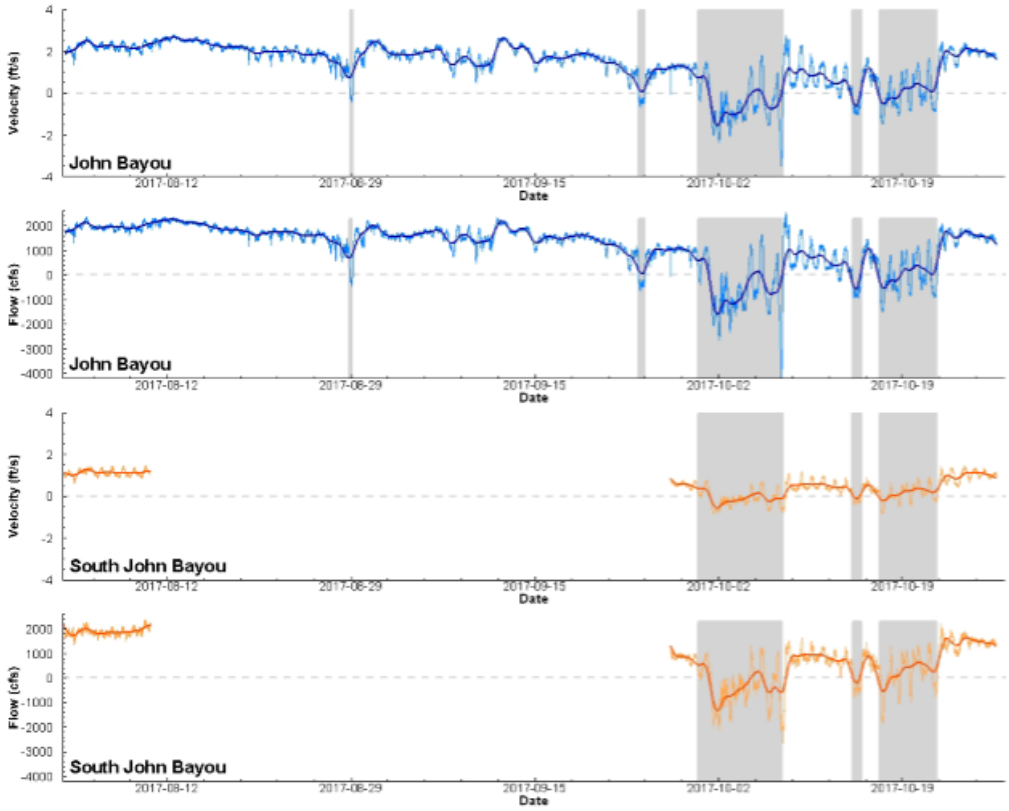

Figure 6.
(Blue) Calculated flow and measured velocity in John Bayou. (Orange) Calculated flow and measured velocity in Fucich Bayou (shown here as South John Bayou). (Gray) Times of flow reversals (Georgiou & Yocum, 2018).

In a study by Nienhuis, Törnqvist, and Esposito (2018), the effects of external controls on levee breach response were investigated. They hypothesized that crevasse splay morphology was related to the relative dominance of floodplain erosion versus deposition. This hypothesis was inspired by a formula devised by Hajek and Edmonds (2014) (Equation 1). Their study tested the relative importance of various external controls on levee breach evolution by developing a predictive metric that looks at the relationship between the potential floodplain deposition rate and the floodplain erosion rate.

Equation 1

$$\frac{D}{E} = \frac{\sum_i c_s w_s}{M\left(\frac{\tau}{\tau_{cr}} - 1\right)} = \frac{\sum_i c_s w_s}{M\left(\frac{\rho g h S}{\tau_{cr}} - 1\right)}, \quad \text{if } \tau > \tau_{cr},$$

D = floodplain deposition rate (kg m^{-2} s^{-1}).
E = floodplain erosion rate (kg m^{-2} s^{-1}).
c_s = the initial sediment concentration in the trunk channel (kg m^{-3}).
w_s = the settling velocity (m s^{-1}).
i = grain sizes (sand and mud). Note: all potential floodplain deposition for all grain sizes were summed.
M = the floodplain erosion coefficient (kg m^{-2} s^{-1}).
τ = a bed shear stress (N m^{-2}), approximated as ρghS.
ρ = the water density (kg m^{-3}).
g = acceleration due to gravity (m s^{-2}).
h = the initial water depth in the breach (m).
S = the imposed water surface slope across the domain.
τ_{cr} = the critical shear stress for erosion of the non-vegetated land surface (N m-2).

Discrete simulations on the effects of breach height, water level slope, soil compressibility, vegetation strength, and floodplain erodibility were examined. They found that flow into the floodplain is autogenic and responsive to breach dimensions and floodplain characteristics. Avulsions were observed in model simulations whenever discharged increased beyond model stability, and the floodplain erosion rate exceeded deposition. Across scenarios that demonstrated crevasse splay formation, their lifetimes varied from less than 1 year to over 30 years (duration during which discharge > 10 m^3 s^{-1}) on and their volumes had a range of over six orders of magnitudes (Figure 7) (Nienhuis et al., 2018).

Their results after investigating varying ratios of D/E (Figure 7a) found that if D>>E, relatively quick breach closure occurred, and no crevasse splay is generated (solid green circle in Figure 7). Conversely, if E>>D, avulsions will occur. This is due to the reason that the initial erosion exceeds distal aggradation that can reduce discharge. The sediment imported through the breach, though high in volume, is not retained within the model domain (Nienhuis et al., 2018).

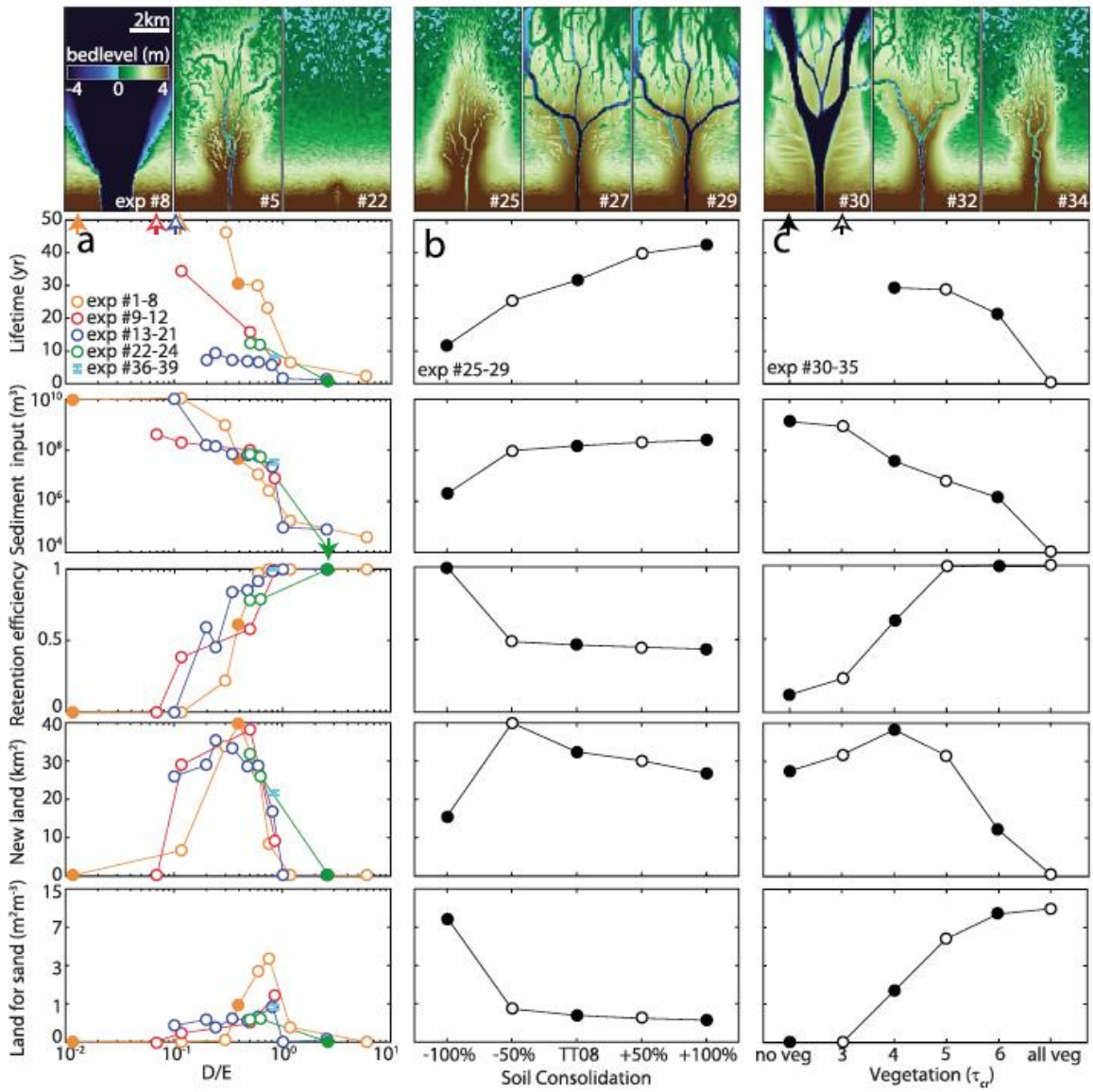

Figure 7.
(Top Row) Floodplain morphology for the experiments after 7 years corresponding with results shown within the same column below. For each column, the effects of (A) D/E ratio (Equation 1), (B) soil consolidation, and (C) vegetation on crevasse splay morphology, splay lifetime, imported sediment volume, fraction retained sediment, new land and the land for your sand. (Arrows) Indicate results plotted outside the domain. Colors within column (A) refer to different sets of experiments among which a characteristic is varied that is included in D, or E. Vegetation is varied between these sets, from high (Blue) to intermediate (Green), to low (Red), to basin vegetation unaffected by water levels (Orange). Vegetation is not represented in Equation 1 for D and E. The range of results from experiments with the varying morphologic scaling factor and grid size is shown as the (Cyan) symbol. All experiments follow the observed soil consolidation rate found by Törnqvist et al. (2008) (Nienhuis et al., 2018).

Crevasse splays form when neither deposition nor erosion dominates (D=E). In this scenario, the initial erosion was influential enough to increase discharge and sediment supply into the floodplain. The simulations showed that harmony was achieved between the volume of incoming sediment and the portion of sediment retained. The simulation bearing the largest addition of new land (elevation above +0.5 m) occurred when the D/E~½. At slightly higher ratios, D/E~1, new land was formed most efficiently. For every cubic m of imported sediment, m^{-1}, new land area formed. However, the study completed by Nienhuis et al. (2018) could not succeed in modeling a scenario where erosion and deposition are exactly balanced in stable equilibrium. The balance always succumbed to processes of avulsion or breach closure.

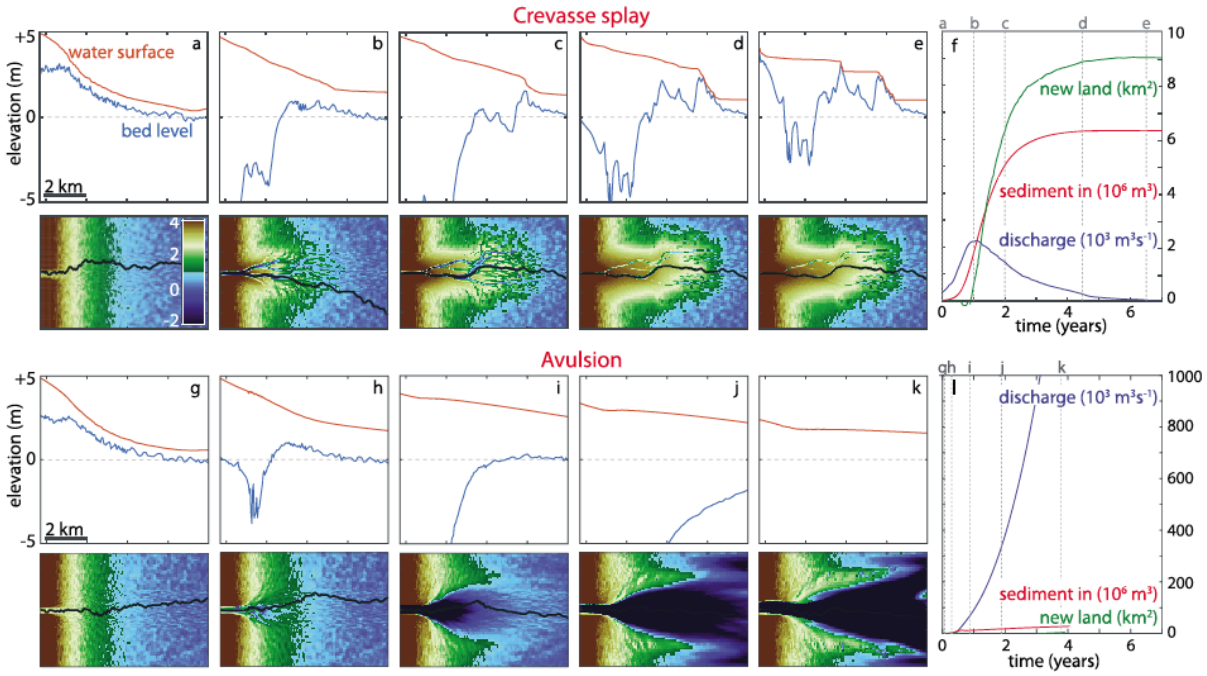

Figure 8.
Evolution of a levee breach forming (A-E) a crevasse splay. (G-K) Evolution of a levee breach forming an avulsion. (Orange) Water surface and (Blue) bed level are shown along the deepest channel (Black Line) on the floodplain. Graphs (F) and (I) depict the growth of new land, imported sediment, and discharge into the floodplain versus time (Nienhuis et al., 2018).

Nienhuis et al. (2018) found that in models that formed crevasse splays, the immediate part of the breach channel eroded. This had the effect of quickly forcing an increase in discharge and inundating the floodplain (Figures 8a and 8b). The associated increase in sediment supply caused deposition across the floodplain, decreasing the local water surface slope at the breach (Figures 8c and 8d). During this phase, new land is formed rapidly, infilling the levee breach with bedload sediments until closure occurred in an average of about 5 years.

Conversely, Nienhuis et al. (2018) created another simulation to outline the conditions sufficient for the formation of an avulsion. One with a more erodible floodplain. In this simulation, erosion of the breach outpaced deposition (Figures 8h and 8i). Here, erosion and discharge increased in concert. Discharge remained high, even though the trunk channel was experiencing a decreasing water surface (Figure 8i). The resulting velocities were so high that it made the model numerically unstable (Nienhuis et al., 2018).

When widespread herbaceous vegetation was factored into crevasse splay building, Nienhuis et al. (2018) found that the vegetation was quickly drowned and lost due to the rising water level (Figure 9, 0.4 years). Afterward, the crevasse jet widened and deposited sediment (1 year). As the bifurcation erosional channels form, the islands in between become vegetated. This vegetation goes on to reduce flow capacity over the islands. This, in turn, further constricts the crevasse splay and lowers water levels (1.3 years) (Nienhuis et al., 2018).

Nienhuis et al. (2018) found that flood plains that are more susceptible to soil consolidation will accommodate splays that contain more sediment and have a longer lifetime. However, in simulations with some soil consolidation greater than zero, the most extensive land area formation was seen.

Vegetation affects the critical shear stress for erosion and the roughness across the vegetated floodplain. Nienhuis et al. (2018) found that by varying the strength of these factors, vegetation can exert a strong control on splay morphology (Figure 7c). In unvegetated simulations, splay morphology is smoother, and floodplains tend to experience avulsions more. The opposite is seen in simulations with heavy vegetation, demonstrating floodplains with more intricate channel patterns. These vegetated floodplains act more efficiently at trapping sediments (Figure 7c) (e.g., Esposito, Shen, Törnqvist, Marshak, & White, 2017; Schumm & Lichty, 1963). Nienhuis et al. (2018) morphodynamic simulations found that intermediate vegetation height and density promoted the highest rate of land growth, in agreeance with simulations of Nardin and Edmonds (2014).

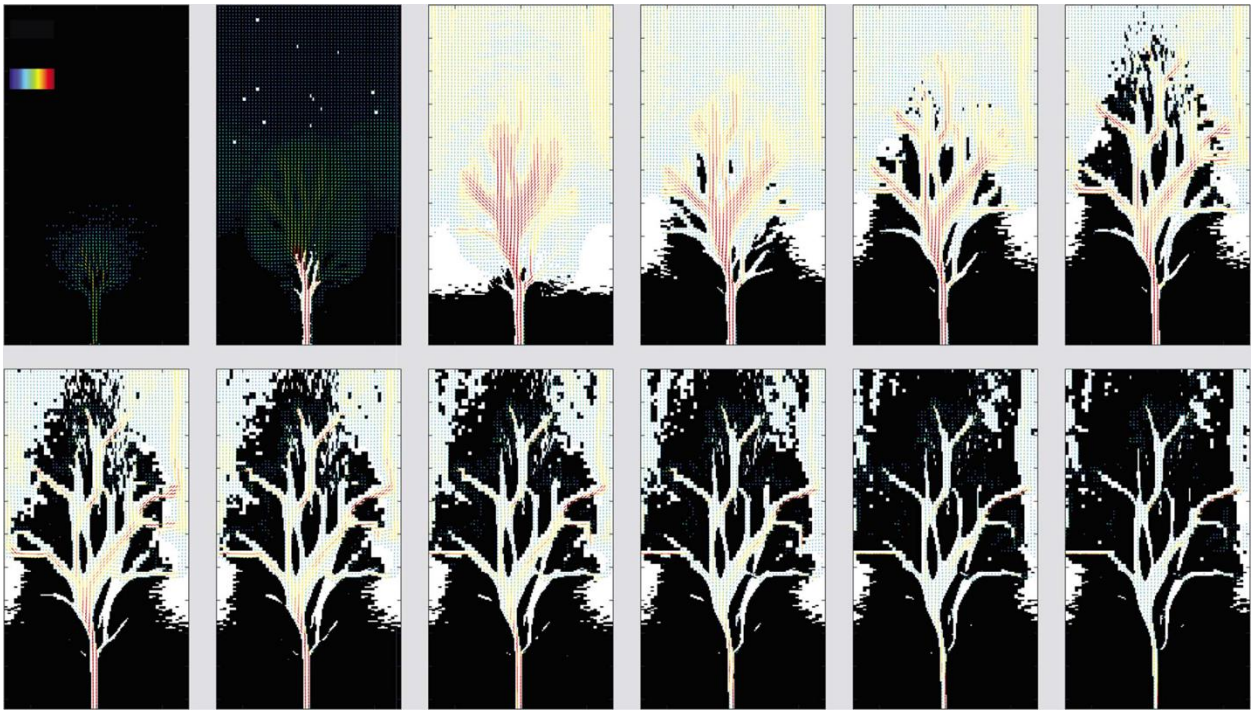

Figure 9.
The coevolution of vegetation, elevation, and flow during the first 3 years of a crevasse splay (Nienhuis et al., 2018).

Hypotheses

H1) With increasing discharge, expanding Mardi Gras Pass channel, and the relatively shorter distance between the Mississippi River and the Gulf of Mexico to its original course, it is likely that Mardi Gras Pass will continue to grow until it connects directly to open water.

H2) The established planform morphology with channelized waterways will help deliver sediment eroded from the developing Mardi Gras Pass farther into the receiving basin.

H3) Tidal and subtidal influences and other receiving basin controls contribute to altering the flow and sediment distribution within the receiving basin and Mardi Grass Pass, facilitating reorganization, which can either accelerate the avulsion timescale or close the breach altogether.

Methods

Planform Metrics

A large database of bathymetry and discharge has developed since the formation of Mardi Gras Pass by the University of New Orleans, Louisiana State University, and NGOs such as the Lake Pontchartrain Basin Foundation (LPBF). Each bathymetry and bank survey was completed using a Trimble Geo Explorer 6000 GeoXR GPS unit along with a Zephyr Model 2 GNSS receiver attached. Utilizing Real-Time Kinematic (RTK) data collection, the professional-grade GPS collected longitude, latitude, and elevation (XYZ) of sub-aerial location with a high degree of confidence. These instruments were coupled with a SonarMite Echo Sounder, the boat-mounted fathometer, so that depth measurements could also be obtained and added to the XYZ data. After collection, these points were imported into GIS and used to create a digital elevation map representing the surface extent of Mardi Gras Pass (Songy et al., 2018).

Field Collection Methods

Field data was collected using vessel-based Acoustic Doppler Current Profiler (ADCP) surveys, instrument deployments, and sediment sampling. A vessel-mounted Teledyne ADCP was used along with a differential global positioning system (DGPS) to collect discharge data throughout the pass. A pre-determined schedule of transects has been followed for each survey (Figure 10). These transects were targeted to establish a flow balance within reach four of MGP (Yocum & Georgiou, 2016). Additional synoptic ADCP measurements were performed to elucidate the distribution of flow throughout the receiving basin. Some areas of interest include the junction of John Bayou with the BLC and the junction of MGP with the BLC. Flow data collected from these synoptic ADCP surveys were used to determine the distribution of flow coming from the MGP into the receiving floodplain.

Figure 10.
Bohemia Survey: Vessel based synoptic ADCP measurement locations courtesy of Georgiou & Trosclair, 2013.

Three Nortek Aquadopp Profilers and RBR's tide gauges were deployed in John Bayou and the upstream position on the BLC (Figure 11) for thirty-five days beginning on June 29, 2017. The Aquadopp Profilers recorded flow and water measurements at 10-minute intervals for two minutes at 2 Hz. The RBRs recorded water level measurements at 10-minute intervals for five minutes at 2 Hz (Georgiou & Yocum, 2018).

Sediment samples were obtained via surface water samples and grab samples. These sediment samples were used to provide total suspended solids (TSS) measurements and grain size distributions. Instrument deployments gathered data on temperature, water level, turbidity, and current profiles (Yocum & Georgiou, 2016).

Figure 11.
(Stars) Represent Nortek Aquadopp Profilers and RBR's tide gage deployment locations. Note that the waterway labeled "Back Levee Canal" is technically Fucich Bayou south of the junction with John Bayou.

Hydrodynamic Data Collection

Velocity data collected from the Aquadopp Profilers and the vessel based ADCP surveys have been used to calculate jet momentum flux using methods developed by Edmonds and Slingerland (2007). The data was also used to infer shear velocities associated with the initiation of sediment motion following the methodology created by Parker, Toro-Escobar, Ramey, and Beck (2003), and Shaw, Mohrig, and Whitman (2013).

Discharge data from ADCP measurements within MGP was compared to daily stage height data from the Mississippi River gage at West Pointe A La Hache (USACE 01400) to create a rating curve for 2017. Hourly tide recordings for 2017 were taken from the nearby Cow Bayou at American Bay near Pointe A La Hache tide gage (USGS 073745258). Storm surge from a few extra-tropical storms and Hurricane Nate are present in the record.

Sediment Distribution

Total suspended solids and turbidity samples were acquired on May 18, May 25, June 29, August 2, and October 27, 2017. Each collection visit followed a programmed route to collect 32 TSS samples and 63 turbidity samples from the predetermined waypoints featured in Figure 12. The collection bottles used for every sample were rinsed three times before filling, and samples were stored on ice until analyzed. Turbidity samples were collected by filling three, 120 ml bottles with surface water at each site. These samples were then analyzed using a Hach 2100P Turbidimeter within 24 hours of collection. Following the analyses, an average was calculated for each site. To collect TSS samples, 1-liter bottles were filled with surface water at each site.

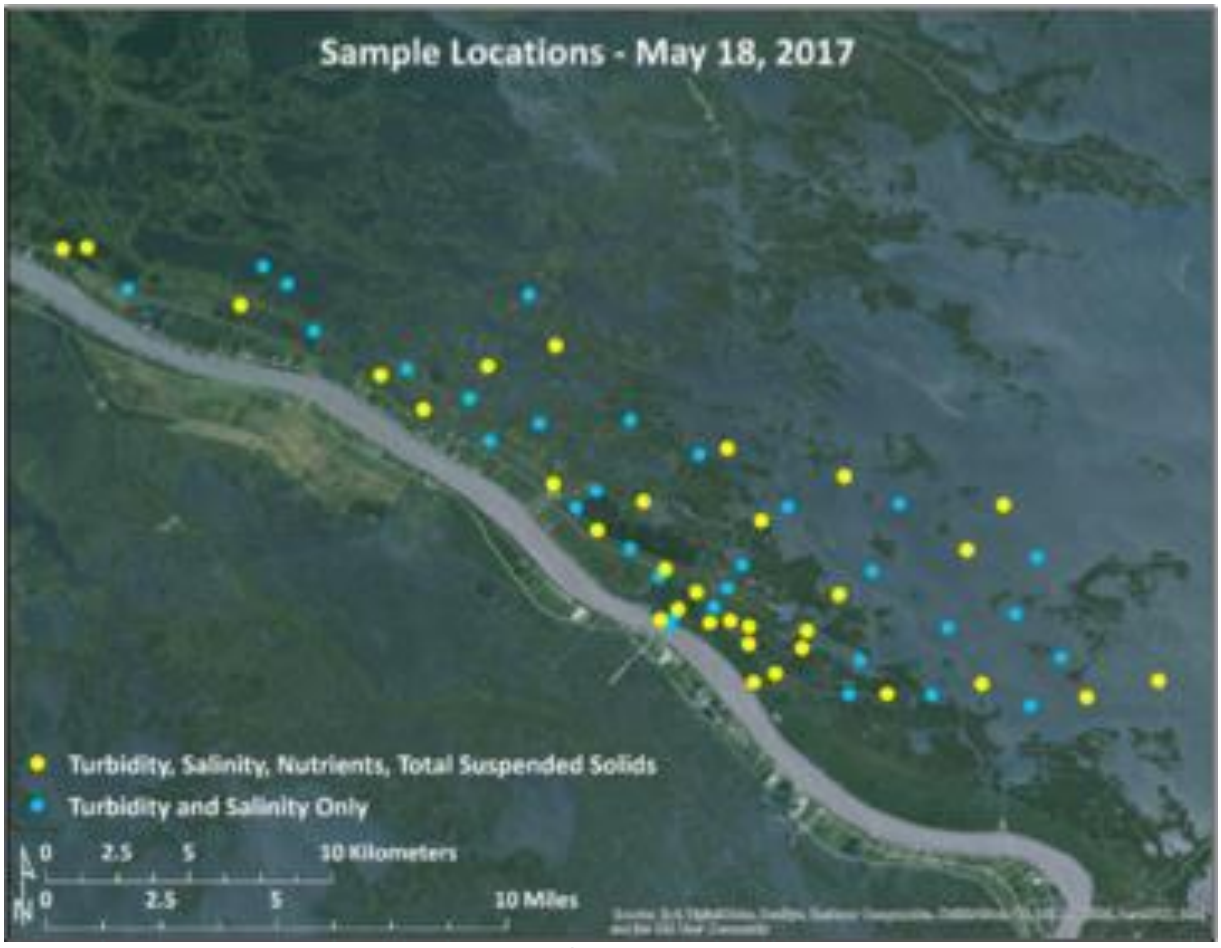

Figure 12.
May 18, 2017, sampling locations. (Yellow) Represents locations sampled for turbidity, salinity, nutrients, and TSS. (Blue) Represents locations sampled for turbidity and salinity only.

TSS analysis of each sample was completed using the methodology described in the *Standard Test Methods for Determining Sediment Concentration in Water Samples* (ASTM D 3977-97). To acquire the suspended sediment concertation (SSC), each sample was siphoned through a pre-weighed 47 mm hydrophilic glass fiber filter with a 0.7 µm pore size (Henkel et al., 2018).

Numerical Modeling

A simulation of floodplain morphology in response to crevasse splaying utilizing the morpho- and hydrodynamic model, Delft3D (Deltares, 2014), was developed. Using the conversion of mass and momentum principles, Delft3D calculates the depth-integrated equations of motion (Lesser, Weis, Patterson, & Jokiel, 1994; Deltares, 2015). Suspended sediment transport (SST) is calculated using a depth-averaged version of 3D advection-diffusion equation:

Equation 2

$$\frac{\partial c_i}{\partial t} + \frac{\partial u_x c_i}{\partial x} + \frac{\partial u_y c_i}{\partial y} + \frac{\partial (u_z - w_{s,i}) c_i}{\partial z} = \frac{\partial}{\partial x}\left(\varepsilon_{s.x.i} \frac{\partial c_i}{\partial x}\right) + \frac{\partial}{\partial y}\left(\varepsilon_{s,y,i} \frac{\partial c_i}{\partial y}\right) + \frac{\partial}{\partial z}\left(\varepsilon_{s,z,i} \frac{\partial c_i}{\partial z}\right)$$

c_i = mass concentration of the sediment fraction (kg m^{-3}), assumes a standard Rouse profile concentration gradient.
u_x,u_y, and u_z, are the directed fluid velocities (m s^{-1})
$w_{s,i}$ = the setting velocity of the sediment fraction (m s^{-1}),
$\varepsilon_{s,x,i}$, $\varepsilon_{s,x,i,}$ and $\varepsilon_{s,x,i}$ are directional eddy diffusivities of the sediment fraction (m^2 s^{-1})

Stokes' law for cohesive sediments is used to set settling velocities, ignoring the effects of flocculation. For noncohesive sediments, settling velocities are set to Van Rijn (1993) depending on the grain diameter:

Equation 3

$$w_{s,i} = \begin{cases} \frac{RgD_i^2}{18\nu}, & 64\,\mu m < D_i < 100\,\mu m \\ \frac{10\nu}{D_i}\left(\sqrt{1 + \frac{0.01RgD_i^3}{\nu^2}} - 1\right), & 100\mu m < D_i < 1000\mu m \\ 1.1\sqrt{RgD_i}, & 1000\mu m < D_i \end{cases}$$

R = the submerged specific gravity (ρ_s ρ_w^{-1}),
ρ_s = the specific density of sediment (kg m^{-3}),
ρ_w = the specific density of water (kg m^{-3}),
g = the acceleration due to gravity (9.81 m s^{-2})
D_i = the grain size diameter of the sediment fraction (m)
v = the kinematic viscosity coefficient of water (m^2 s^{-1})

Suspended sediment exchange between noncohesive sediments and the bed is calculated as an erosive flux. This is due to sediment settling, causing upward diffusion and a depositional flux. The deposition and erosion of cohesive sediments are calculated using the Partheniades-Krone formulations (Partheniades, 1965):

Equation 4

$$F_{e,i}\begin{cases}\left(\frac{\tau_0}{\tau_{ce(C)}}-1\right), & when\ \tau_0 > \tau_{ce(C)}\\ 0, & when\ \tau_0 \le \tau_{ce(C)}\end{cases}$$

$$F_{d,i} = W_{s,i}c_{b,i}\begin{cases}\left(\frac{\tau_0}{\tau_{cd(C)}}-1\right), & when\ \tau_0 < \tau_{cd(C)}\\ 0, & when\ \tau_0 \ge \tau_{cd(C)}\end{cases}$$

$F_{e,I}$ and $F_{d,I}$ are erosive and depositional fluxes of the cohesive sediment fraction (kg $m^{-2}s^{-1}$)
τ_o = the bed shear stress (N m^{-2})
$\tau_{ce(C)}$ and $\tau_{cd(C)}$ are critical shear stresses for erosion and deposition of the cohesive sediment
$c_{b,i}$ = the sediment concentration near the bed of the sediment fraction (kg m^{-3})

The bed level is adjusted accordingly with source and sink terms. The methodology developed by Van Rijn (1993) is used to calculate bedload transport:

Equation 5

$$q_{b,i} = 0.006 w_{s,i} D_i \left(\frac{u(u-u_{c,i})^{1.4}}{(RgD_i)^{1.2}}\right)$$

$q_{b,I}$ = the bedload sediment discharge per unit of the sediment fraction (m^2 s^{-1})
u = the depth-averaged velocity (m s^{-1})
$u_{c,I}$ = the critical depth-averaged velocity (m s^{-1}) for initiation of motion of the sediment fraction

Bedload transport direction is determined by local flow conditions and adjusted for bed-slope effects (Bagnold, 1966; Ikeda, 1982).

Simulation Design

Using Delft3D, a virtual domain was created by integrating the bathymetric and topographic data produced by the LPBF with digital elevation maps compiled by the United States Geological Survey's (USGS) Coastal National Elevation Database (CoNED) (Danielson et al., 2016) (Figures 13 - 15). Three boundaries were necessary for this model (Figure 16). The primary inflow was represented by a time-series total discharge boundary created using the rating curve to force water from the MR into MGP. A discharge and water height (QH) relation boundary was placed at the northern terminus of the BLC to serve as an outflow for water flowing north. Lastly, a time-series water level boundary was placed along the eastern edge of the model to simulate tide observations taken from the Cow Bayou tide gage.

Two sediment fractions were implemented: fine sand and cohesive mud. Both Allison et al. (2012) and Nittrouer et al. (2008) found that roughly 21% of the annual sediment concentration in the lower reach of the Mississippi River is sand, leaving about 79% as cohesive mud (<63 μm; ϕ>8). This ratio closely matched the ratio found in a 2013 laser in-situ scattering and transmissometry (LISST) analysis using only a sample taken near the upstream boundary of MGP (71% fines, 29% sand) (UNO-PIES, unpublished data). Due to the results' similarity, the ratio put forth by Allison et al. (2012) and Nittrouer et al. (2008) was chosen to represent the ratio of the incoming MR sediment fractions at the MGP boundary.

An average SSC was calculated within the receiving basin from all of the TSS analyses completed in 2017. This average was determined to be 0.09351 kg m^{-3}. The 2017 LISST analyses showed that the average sand to cohesive mud ratio within the receiving basin was approximately 24% and 76%, respectively, similar to the ratio observed from the Mississippi River.

Initially, a month-long hindcast simulation was produced to recreate a MR flood event in 2017 from mid-May to mid-June. This simulation was used in an iterative process to deduce the best parameters for recreating the flood's observed outcomes within MGP and its receiving basin by using the observed flow distributions, discharges, SSC measurements, and water levels to fine-tune the hindcast. A cohesive settling velocity of $7x10^{-6}$ m s^{-1}, combined with a Chezy roughness coefficient of 35 $m^{0.5}$ s^{-1} for both U and V vectors, and a critical bed shear stress for erosion value of 5 N m^{-2}, worked best to replicate the observed SSC values found throughout the floodplain during 2017. These values for the Chezy roughness coefficients and critical bed shear stress for erosion are similar to what Nienhuis et al. (2018) employed when considering vegetated conditions within the floodplain. All Delft3d input parameters can be viewed in Appendix A.

The annual average SSC reaching the Head of Passes, the lowermost point on the MR, was approximately 0.24 kg m^{-3} from 2008-2010 (Allison et al., 2012). However, incoming SSC from the MR was chosen to vary between 0.025 to 0.18 kg m^{-3} depending on the month. This choice was determined because there was a better correlation to observed SSC within the floodplain than the concentration put forth by Allison et al. (2012). This lower concentration could be because MGP only captures a fraction of the Mississippi River, with its initial thalweg depth considerably higher than the bottom of the Mississippi River at that locale. Therefore, uniform delivery of suspended sediment should not be expected.

After the month-long hindcast results proved comparable to observed trends, the parameters iteratively produced were applied to a year-long hindcast of 2017. This year-long hindcast was once again compared to the observed trends for 2017 within MGP and its receiving basin to determine its accuracy, the results of which are outlined later in this paper. This model went on to provide the foundation from which the two following simulations are deployed.

Figure 13.
Observation points are located at all cross-section locations

Figure 14.
Cross-sections throughout the model domain.

Figure 15.
Cross-sections throughout the model domain.

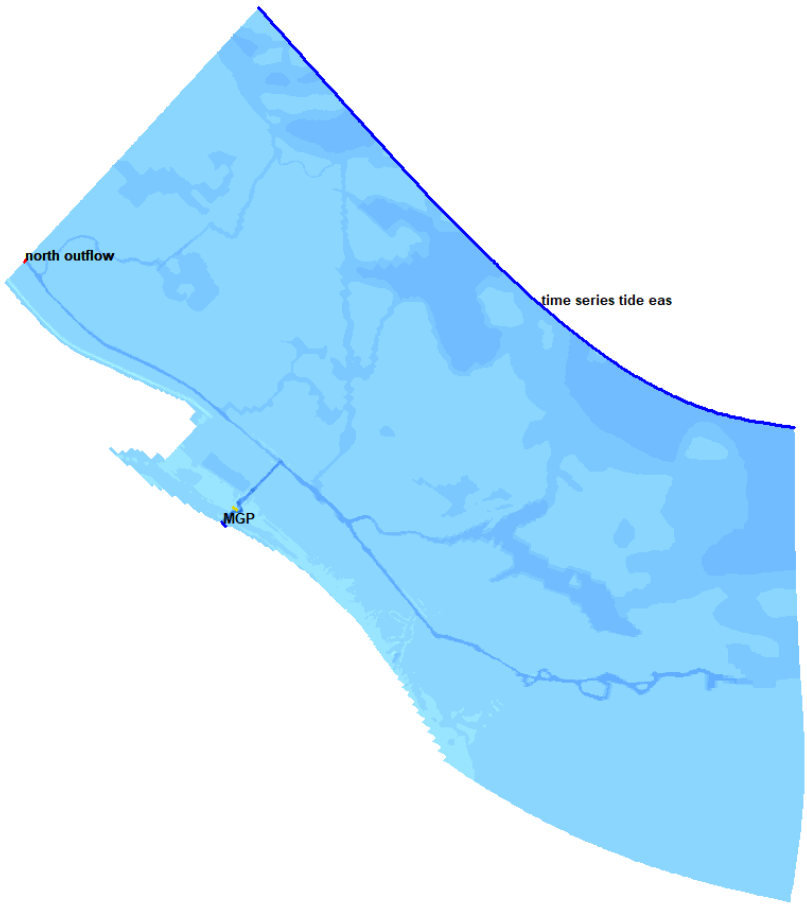

Figure 16.
The full model domain and the location of boundaries.

Hydrodynamic Analysis

To analyze storm surge and tide's effect on MGP and surrounding floodplain, an alternative version of the hindcast simulation was created, without subtidal and tidal influence. Water level, flow and sediment transport measurements taken from cross-sections and observation points within the two models were compared to one another. Georgiou & Yocum (2018) reported that tidal and subtidal forces have an influence on river discharge within the study area. It is expected that these tidal and subtidal forces and their consequences will affect channel network geometry for MGP and the floodplain.

20-Year Forecast

This forecast attempted to demonstrate how MGP and its receiving basin will react to the continuing influx of MR discharge and relative sea-level rise (RSLR) over the next 20 years. The model has a morphological scale factor of 20 that will force the 1-year simulation to replicate 20 years of morphological dynamics. Intermediate scenario RSLR for Grande Isle, LA, the nearest forecasted station, is expected to rise approximately +0.57 m over the next 20 years (Sweet, Kopp, Weaver, Obeysekera, Horton, Thieler, & Zervas, 2017). Linear interpolation between 0 and +0.57 m was used to create a vector that contained the same number of elements that comprised the hourly tide gage's water level record for 2017. The elements of the two vectors were then added together and used for the tidal boundary to simulate the projected RSLR.

Hindcast Accuracy

The hindcast was analyzed at observation points and cross-sections at key locations shown in Figures 13 - 15, against conditions observed throughout 2017 at MGP and its receiving basin (Table 1) to determine the accuracy of the hindcast to replicate discharge, flow distribution and SSC throughout the domain. The analysis showed that discharge through MGP was fairly accurate throughout the year (Table 1). This strong correlation continued as water exited MGP and flowed to the North and South during the first half of the year, where higher discharge is present. However, this correlation weakened from August on (Table 1). This decoupling is likely due to how the hindcast was initially developed during flood conditions.

Accuracy of the southerly flow is higher than the northerly flow, as demonstrated in Table 1. Partition of the flow north and south as it exited MGP was observed to average 36% to the North, and 63% to the South. The simulation closely matched this distribution, with 39% flowing north, and 61% flowing south.

As flow approached the junction of John Bayou and the BLC, the simulated discharge was consistently lower compared to observations, as shown in Table 2. It appears that the QH-relationship of the North BLC outflow boundary generated a higher outflow than what was observed. Despite this, flow distribution leaving MGP, and at the BLC-JB junction was maintained. The averaged simulated partition of from the BLC into John Bayou, and Fucich Bayou (JB: 54%; FB: 43%) closely resembled observed values (JB: 58%; FB: 49%).

Originally, the North BLC outflow boundary was designated as a total discharge boundary, using a rating curve developed by utilizing ADCP measurements near that boundary to ADCP measurements at the end of MGP. However, this, too, had an erroneous effect on the simulation by reversing flow within Lower Grand Bayou. Despite this, the instantaneous discharge at the JB-BLC split was more agreeable to observed conditions (Table 3). When the results from these two simulations were compared, the QH-relation boundary condition appears to have increased cumulative total sediment transport through the Northern BLC boundary from 52.67 thousand-tonnes to 85.63 thousand-tonnes per annum. In other words, of the incoming MR suspended sediment flux, the amount exiting the domain annually via the North BLC terminus went from 20% to 32%. It was meanwhile reducing total sediment transport south through the JB-BLC junction from 103.8 thousand-tonnes to 85.53 thousand-tonnes per annum, decreasing the junction's share of the initial MR sediment budget transported from 39% to 33%.

Suspended sediment concentrations exiting MGP showed good agreement with observations during the first half of the year but departed as the year progresses. As explained earlier, this is likely due to how the model was iteratively developed. This SSC trend is seen in both observation points immediately north and south of the end of MGP (Table 1). The error in discharge and SSC rises with increasing distance from MGP (Table 2).

The model was run with dynamic bathymetry updating. The simulated erosion and deposition trends were compared to observed morphological trends throughout MGP from November 2016 to November 2017 (Cretini et al., 2016; Songy et al., 2018). The hindcast tended to follow observed trends within the center of MGP. However, observation points located at the entrance and exit of MGP recorded deposition rather than erosion (Table 4).

Obversation Point: End of Mardi Gras Pass (MGP_END)								
	Dishcarge							
		18-May	25-May	29-Jun	2-Aug	27-Sep	27-Oct	AVG
Cubic Meters per Second	Q	375.4	400.0	292.5	190.4	142.1	139.9	256.7
	Observed Q	385.8	407.7	297.3	190.1	142.8	138.3	260.3
	RMSE	10.4	7.7	4.8	0.3	0.7	1.6	4.2
	MAPE %	2.69%	1.90%	1.62%	0.14%	0.48%	1.15%	1.33%
Obversation Point: South of Mardi Gras Pass (SoMGP)								
Fraction		**Suspended Sediment Concentration**						
		18-May	25-May	29-Jun	2-Aug	27-Sep	27-Oct	AVG
Kilogram per Cubic Meter	Sand	2.9E-02	4.1E-02	8.9E-03	4.6E-06	9.2E-09	3.3E-07	1.3E-02
	Cohesive	1.4E-01	1.4E-01	9.9E-02	7.1E-02	2.4E-02	3.1E-02	8.4E-02
	Total	1.7E+02	1.8E+02	1.1E+02	7.1E+01	2.4E+01	3.1E+01	9.8E+01
	Observed	1.8E+02	1.8E+02	1.2E+02	9.5E+01	2.9E+01	4.4E+01	1.1E+02
	RMSE	7.6E+00	5.3E+00	1.1E+01	2.4E+01	5.0E+00	1.3E+01	1.1E+01
	MAPE %	4.28%	3.00%	9.41%	25.42%	17.45%	29.83%	15%
	Dishcarge							
Cubic Meters per Second	Q	261.1	278.7	197.6	117.4	77.2	72.3	167.4
	Observed Q		252.8	206.0		116.0	85.0	164.9
	RMSE		25.9	8.4		38.8	12.7	21.4
	MAPE %		10.27%	4.06%		33.43%	14.95%	15.67%
Obversation Point: North of Mardi Gras Pass (NoMGP)								
Fraction		**Suspended Sediment Concentration**						
		18-May	25-May	29-Jun	2-Aug	27-Sep	27-Oct	AVG
Kilogram per Cubic Meter	Sand	1.9E-02	2.7E-02	5.8E-03	2.3E-04	1.0E-08	1.5E-03	8.9E-03
	Cohesive	1.4E-01	1.4E-01	9.8E-02	7.0E-02	2.4E-02	3.1E-02	8.4E-02
	Total	1.6E+02	1.7E+02	1.0E+02	7.0E+01	2.4E+01	3.3E+01	9.3E+01
	Observed	1.7E+02	1.7E+02	1.2E+02	7.8E+01	1.5E+01	2.6E+01	9.6E+01
	RMSE	1.1E+01	2.7E+00	1.4E+01	7.3E+00	8.1E+00	6.9E+00	8.3E+00
	MAPE %	6.39%	1.57%	11.90%	9.38%	52.73%	26.78%	18%
	Dishcarge							
Cubic Meters per Second	Q	119.4	124.4	96.7	74.1	65.7	67.5	91.3
	Observed Q		160.6	118.0		55.8	42.0	94.1
	RMSE		36.2	21.3		9.9	25.5	23.2
	MAPE %		22.52%	18.01%		17.82%	60.79%	29.79%

Table 1.
Comparison of simulated discharge and SSC during the 1-year hindcast to observed values at cross-sections.

Obversation Point: JB_BLC Junction								
Fraction		Suspended Sediment Concentration						
		18-May	25-May	29-Jun	2-Aug	27-Sep	27-Oct	AVG
Kilogram per Cubic Meter	Sand	1.3E-04	4.7E-04	1.9E-06	3.5E-11	2.2E-10	3.1E-14	1.0E-04
	Cohesive	1.4E-01	1.4E-01	9.7E-02	6.8E-02	2.2E-02	3.0E-02	8.3E-02
	Total	1.4E+02	1.4E+02	9.7E+01	6.8E+01	2.2E+01	3.0E+01	8.3E+01
	Observed Total	2.5E+02	2.2E+02	1.2E+02	5.8E+01	2.2E+01	3.5E+01	1.2E+02
	RMSE	1.1E+02	8.4E+01	2.7E+01	1.0E+01	2.7E-01	4.5E+00	4.0E+01
	MAPE %	44.74%	37.37%	21.82%	18.13%	1.23%	13.03%	23%
	Dishcarge							
Cubic Meters per Second	Q	170.3	185.3	124.1	69.0	42.3	42.5	105.6
	Observed Q		234.7	189.6	104.7		79.0	152.0
	RMSE		49.4	65.5	35.7		36.5	46.8
	MAPE %		21.07%	34.56%	34.12%		46.19%	33.98%
Obversation Point: John Bayou (JB)								
Fraction		Suspended Sediment Concentration						
		18-May	25-May	29-Jun	2-Aug	27-Sep	27-Oct	AVG
Kilogram per Cubic Meter	Sand	1.6E-04	2.6E-04	1.1E-06	-3.2E-17	2.7E-24	4.3E-12	7.1E-05
	Cohesive	1.4E-01	1.4E-01	9.6E-02	6.7E-02	2.1E-02	3.0E-02	8.2E-02
	Total	1.4E+02	1.4E+02	9.6E+01	6.7E+01	2.1E+01	3.0E+01	8.2E+01
	Observed	2.5E+02	1.9E+02	1.2E+02	7.0E+01	2.3E+01	4.2E+01	1.2E+02
	RMSE	1.1E+02	5.1E+01	2.4E+01	2.2E+00	1.2E+00	1.3E+01	3.3E+01
	MAPE %	43.62%	26.73%	19.83%	3.16%	5.28%	29.80%	21%
	Dishcarge							
Cubic Meters per Second	Q	101.0	100.0	79.9	31.0	12.3	14.9	56.5
	Observed Q		163.1	98.1	53.0		40.0	88.6
	RMSE		63.1	18.2	22.0		25.1	32.1
	MAPE %		38.67%	18.54%	41.48%		62.69%	40.35%
Obversation Point: Fucich Bayou								
Fraction		Suspended Sediment Concentration						
		18-May	25-May	29-Jun	2-Aug	27-Sep	27-Oct	AVG
Kilogram per Cubic Meter	Sand	1.8E-06	6.7E-06	2.7E-09	-2.0E-18	2.5E-19	1.4E-22	1.4E-06
	Cohesive	1.4E-01	1.4E-01	9.7E-02	6.8E-02	2.2E-02	3.0E-02	8.3E-02
	Total	1.4E+02	1.4E+02	9.7E+01	6.8E+01	2.2E+01	3.0E+01	8.3E+01
	Observed Total	2.1E+02	7.5E+01	1.0E+02	6.9E+01	2.7E+01	3.5E+01	8.5E+01
	RMSE	6.5E+01	6.5E+01	3.6E+00	1.2E+00	5.4E+00	5.0E+00	2.4E+01
	MAPE %	31.92%	86.15%	3.63%	1.74%	19.86%	14.30%	26%
	Dishcarge							
Cubic Meters per Second	Q	75.6	80.8	54.2	28.8	17.2	13.0	44.9
	Observed Q		113.0	91.6	51.2		42.0	74.5
	RMSE		32.2	37.4	22.4		29.0	29.5
	MAPE %		28.53%	40.82%	43.84%		69.07%	39.66%

Table 2.
Comparison of simulated discharge and SSC during the 1-year hindcast to observed values at cross-sections near John Bayou and Fucich Bayou Junction.

JB_BLC SPLIT Discharge (m^3/s)							
Date	18-May	25-May	29-Jun	2-Aug	27-Sep	27-Oct	AVG
Q	185.1	199.6	143.8	90.0	65.4	66.1	125.0
Observed Q		234.7	189.6	104.7		79.0	152.0
RMSE		35.1	45.8	14.7		12.9	
MAPE %		14.97%	24.17%	14.07%		16.39%	

Table 3.

A table of discharge rates at the BLC-JB junction from a simulation using a total discharge boundary type at the northern end of the BLC. The final version of the simulation used a QH-relation type boundary. Compare this table to Table 2 to assess the difference the different boundary type conditions may have had on the simulation.

Mardi Gras Pass Thalweg Depth Comparison: Simulated vs. Observed (ft)				
Observation Point	Nov-16	Jan-17	Nov-17	Dec-17
Simulated MGP_END		26.2	23.3	23.3
Observed MGP_END	23.5		26.6	
Simulated 3/4 MGP		20.3	24.9	25.5
Observed 3/4 MGP	20.4		24.1	
Simulated After Bend		19.4	22.8	24.7
Observed After Bend	19		23.05	
Simulated Before Bend		45.6	34.9	35.8
Observed Before Bend	40		48	

Table 4.

Comparison of thalweg depths between observed and simulated conditions at the various cross-sections used in the model (Cretini et al., 2016; Songy et al., 2018).

Results

Tidal and Subtidal Influence

The 1-year simulation conducted without tidal and subtidal influences was compared to the 1-year hindcast simulation. Tidal and subtidal forcing were found on average to increase water levels by 57% at the end of MGP (Figure 17). Meanwhile, those forces increased water levels at the BLC – John Bayou junction by only 24% (Figure 18).

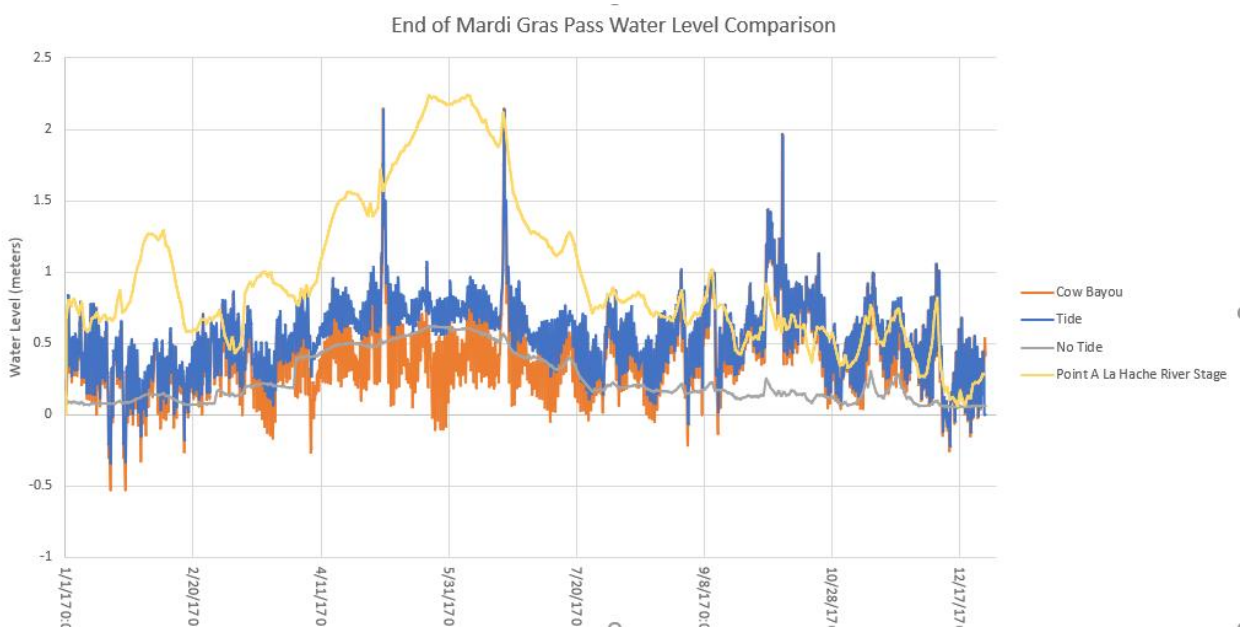

Figure 17.
Water level comparison at the end of MGP with and without tidal & subtidal influences.

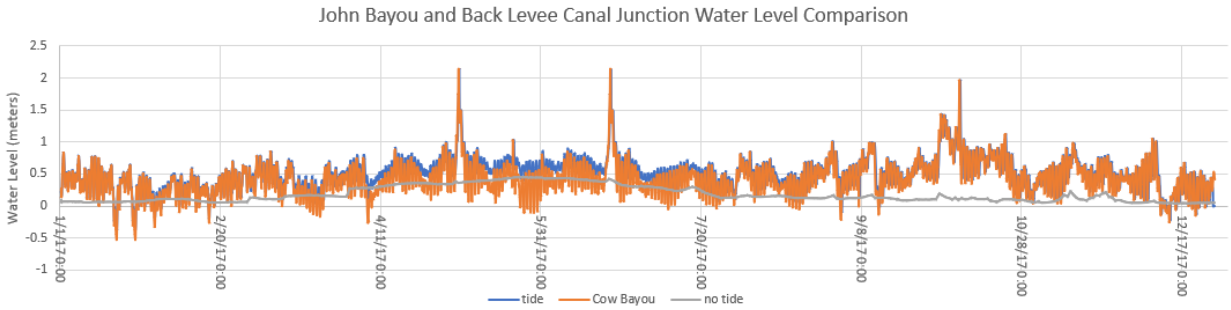

Figure 18.
Water level comparison at the junction of Back Levee Canal and John Bayou with and without tidal and subtidal influences.

Water levels at the end of MGP, without tidal or subtidal influence, never exceeded 0.62 m, while the average water level was approximately 0.24 m. Water levels higher than 0.59 m only occurred when the river stage at West Pointe A La Hache was at least 2 standard deviations (std dev = 0.538 m) higher than the 2017 average of 0.96 m.

Water levels at the end of MGP varied throughout the year, responding to tidal, subtidal, river and storm influences. They typically rose above 1 m whenever the tide was 1.66 standard deviations from the mean, and the river stage was at least above 1 standard deviation below the mean. Whenever the river stage was over 2 standard deviations above the mean, and tide levels were above 0.77 m, water levels at the end of MGP over 1 m was achieved. The maximum level recorded was 2.18 m, while the average was approximately 0.96 m, and the standard deviation was about 0.54 m. Water levels nearing or exceeding 1 m were recorded occurring for a total of 10.8 days throughout the hindcast. Of those instances, a total of 6.1 days (56%) were recorded when the river stage was within a standard deviation below the mean water level (0.43 m to 0.96 m), and when the tide was greater than 1 standard deviation from the mean (avg = 0.43; std dev = 0.267 m). The remaining 4.8 days occurred when the river stage was greater than or equal to the mean and when tide levels were at a minimum of 0.87 m.

Typically, the tide level at Cow Bayou is lower than the river stage at West Pointe A La Hache, signaling the gradation from estuarine to fluvial conditions. However, storm surge had a significant effect on water levels and flow direction. Hurricane Nate occurred during low river stage, and the storm surge produced was higher than the river. The data produced from the event was useful in simulating the impact of hurricanes on the study area. The storm surge at Cow Bayou reached its peak at 1.44 m. The average river stage was 0.87 m, less than the mean stage. Hurricane Nate induced storm surge that caused the flow to reverse within MGP for about 1 hour and 24 minutes. During the hurricane, the flow reversed in the BLC south of MGP for approximately 9 hours and 24 minutes. Back Levee Canal flow reversal occurred during three other events for a total of 5 hours and 36 minutes throughout the hindcast.

Beyond Hurricane Nate, the water level in Cow Bayou was higher than the MR 15.4% of 2017. From January to the end of June, water levels in Cow Bayou exceeded the MR only 1.5% of the time. From July to the end of December, water levels in Cow Bayou were higher than the MR 13.8% of the time.

At the end of MGP, the maximum tide level was recorded at 2.18 m, and the minimum tide level was recorded at -0.34 m, a 275% difference. During flood conditions, the tidal range was shown to have a reduced amplitude when compared to when river stage levels are relatively low. For instance, during the late May, early June flood, the spring tide was 1.08 m, and the neap tide was 0.56 m at the end of MGP, a 64% difference. However, during January, when the river stage was low, spring tide was 0.84 m, and the neap was -0.34 m, a 477% difference in amplitude (Figure 19).

Tidal and subtidal influences were shown to have a small effect on hindering SSC immediately north and south of MGP, and at the John Bayou - BLC junction, reducing SSC by an average percent difference of 0.6%, 2.5%, and 1.6%, respectively (Table 5).

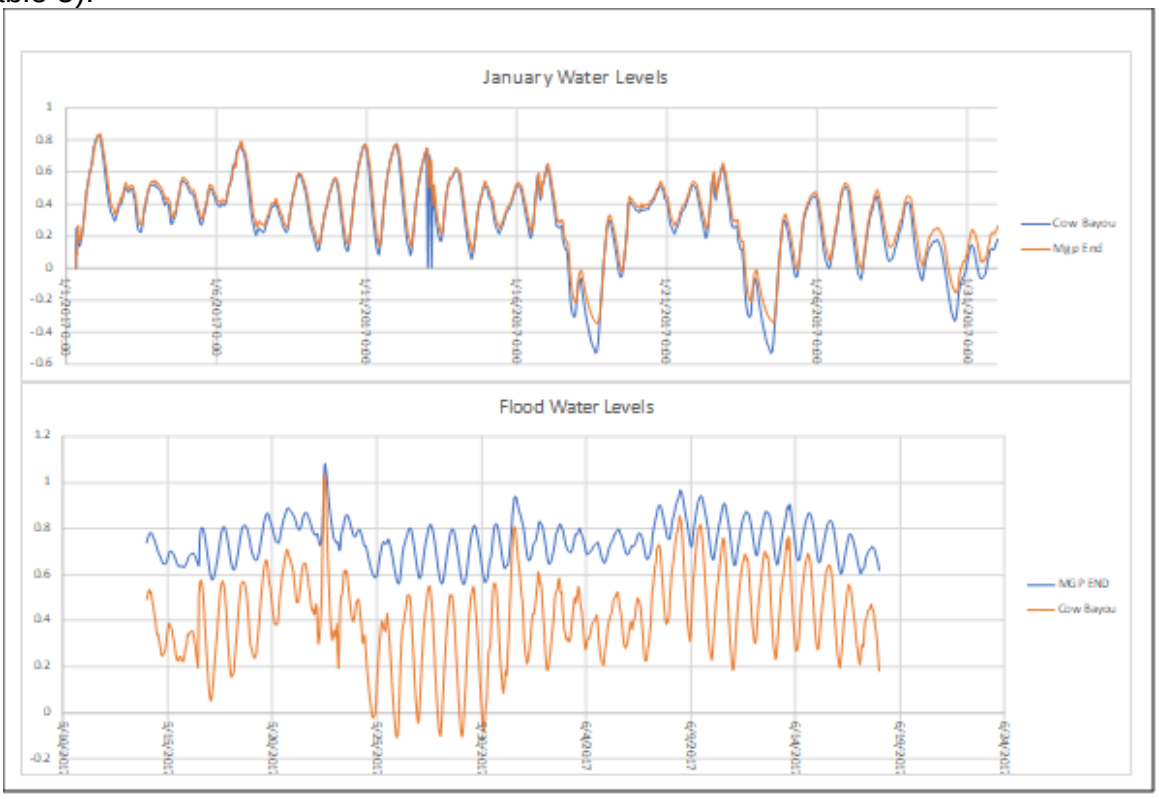

Figure 19.
Comparison of water levels during a low water episode (above) and a flood event (below).

Average SSC: Both Fractions (kg m^{-3})			
	NoMGP	SoMGP	JB-BLC
With Tidal/Subtidal Influences	3.92E-02	3.96E-02	3.64E-02
No Tidal/Subtidal Influences	3.90E-02	4.06E-02	3.69E-02
Difference	2.27E-04	-9.96E-04	-5.71E-04
% Difference	0.6%	2.5%	1.6%

Table 5.
Comparison of the suspended sediment concentration leaving Mardi Gras Pass and at the junction of where the Back Levee Canal meets John Bayou during the 1-year hindcast and the 1-year simulation executed without tidal or subtidal influences.

At the end of Mardi Gras Pass, tidal and subtidal influences reduced instantaneous discharge on average of 5%. Tidal and subtidal forcing increased instantaneous discharge inland by 29% on average, along the North BLC, while reducing discharge to the South BLC by an average of 44%. Tidal and subtidal forces reduced instantaneous discharge at the JB and FB cross-sections on average by 52% and 50%, respectively.

However, tidal and subtidal forces were shown to have increased the amount of sediment retained within the floodplain (Table 6). Without tidal or subtidal forces, 31% of MR sediment flux was retained in the floodplain. With tidal and subtidal forces, retention was increased by up to 42%. Considering the North BLC terminus QH-boundary's expediting effect on increasing sediment flux out of the domain, it could be extrapolated that approximately 50% of the incoming MR sediment would be retained, further supporting the importance of tidal and subtidal forces on increasing sediment retention within the receiving basin.

Cumulative Total Transport (m^3)		
Cross-Section	No Tide	With Tide
BLC N Terminus	13%	32%
LGB	4%	1%
JB	20%	17%
Fucich End	17%	8%
Clam Bay	15%	
Leaving Floodplain	69%	58%
Retained	31%	42%

Table 6.

Comparisons of cumulative total volumetric transport for simulations with and without tides. The cumulative volume of sediment that passes each of the following cross-sections, which can be considered as exits from the floodplain, is compared to the cumulative volume that passes through the beginning of Mardi Gras Pass.

Tidal and subtidal forces were shown to alter flow distribution considerably. Without these forces, flow north from MGP went from capturing 39% of the flow, to only capturing 28% of the flow on average. Whereas, the flow south of MGP increased from 61% to 72% of the flow on average. Further away from the Mississippi River, flow through JB and FB were reduced a percentage point, from 57% to 56%, and from 45% to 44%, respectively. It is clear that tidal and subtidal forces have little effect on the flow distribution between JB and FB.

20-Year Forecast

Planform Morphology

As the forecast began, bank overtopping started immediately in MGP. Several breaches occurred throughout MGP during high flow. Initially, the overtopping discharge flowed to the North; however, flow to the South began in March. This overtopping scoured new, smaller channels, emanating from MGP for water to exit. However, only one of these breaches had significant long-term effects on MGP. The breach occurred on the northern bank of MGP, initially connecting to the adjacent pond seen in Figure 20A, and continuing to short-circuit the BLC. This new channel connected with the BLC directly opposite of where an existing channel goes on to connect with Clam Bay. This route ultimately flows to open water via Bayou Law. The outlet dimensions of this breach do not incise to depths similar to the proximal channel depth in MGP. Although, with increasing distance downstream, the breach's depth tended to converge to the proximal channel depth in MGP.

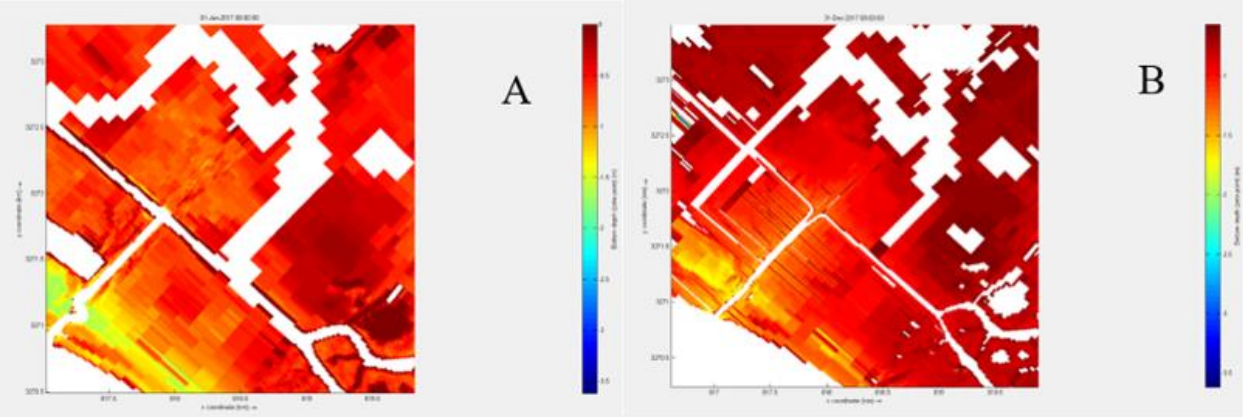

Figure 20.
(A) Mardi Gras Pass at the beginning of the forecast. (B) Final topography produced from the 20-year forecast.

The meander near the headwaters of MGP straightened in the latter half of March. Deposition occurred around the thin dam placed there to represent an existing culvert structure until the MGP migrated to the southeast, and a straight channel was developed (Figures 20B & 21).

At the beginning of April, deposition at the mouth of MGP disconnected the BLC (Figures 16B & 22). After 20 years, the portion of MGP upstream from the newly built mouth bar that divided the BLC expanded from roughly 45 m to 69 m. Both sections of the BLC experienced significant lateral accretion. Channel width was reduced from about 80 m to 30 m in the BLC north from MGP. This trend was observed for approximately 3100 m north from MGP. Halfway between MGP and the BLC-JB junction, the channel narrowed from about 70 m to 45 m. At the junction, the channel width was reduced from about 100 m to 55 m. This phenomenon continued briefly along John Bayou and Fucich Bayou to the South.

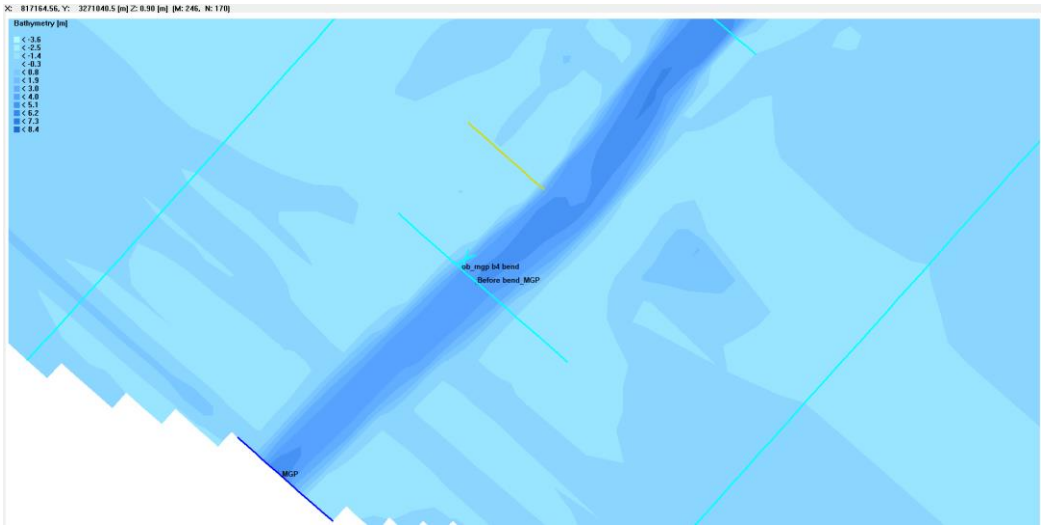

Figure 21.
The locations of some cross-sections (light blue lines), observation points (light blue crosses), inflow boundary (dark blue line), and thin dam (yellow line) are super positioned above a bathymetry image taken from the last day of the 20-year forecast.

Figure 22.
The locations of cross-sections (lines) and observation points (crosses) super positioned over a bathymetric image taken from the last day of the 20-year forecast.

At the end of the forecast, a net loss of land was evident (Figures 23 and 24). However, there were instances of land building near the channels. In addition to the terminal mouth bar and straightening that occurred within MGP, most new land was produced from lateral accretion within the BLC and MGP. The majority of accretion throughout the forecast lied within the channels. Cumulative erosion and deposition within the domain at the end of the forecast are exhibited in Figure 25. Channel bed erosion occurred in John Bayou before the channel widens to open water. Additional erosion occurred in the area between mid-MGP and north BLC as the channel migrated (Figure 25). Also significant was the amount of vertical mineral accretion that happened throughout the floodplain (Figure 24). Vertical accretion materialized not only adjacent to the waterways but throughout the marsh platforms.

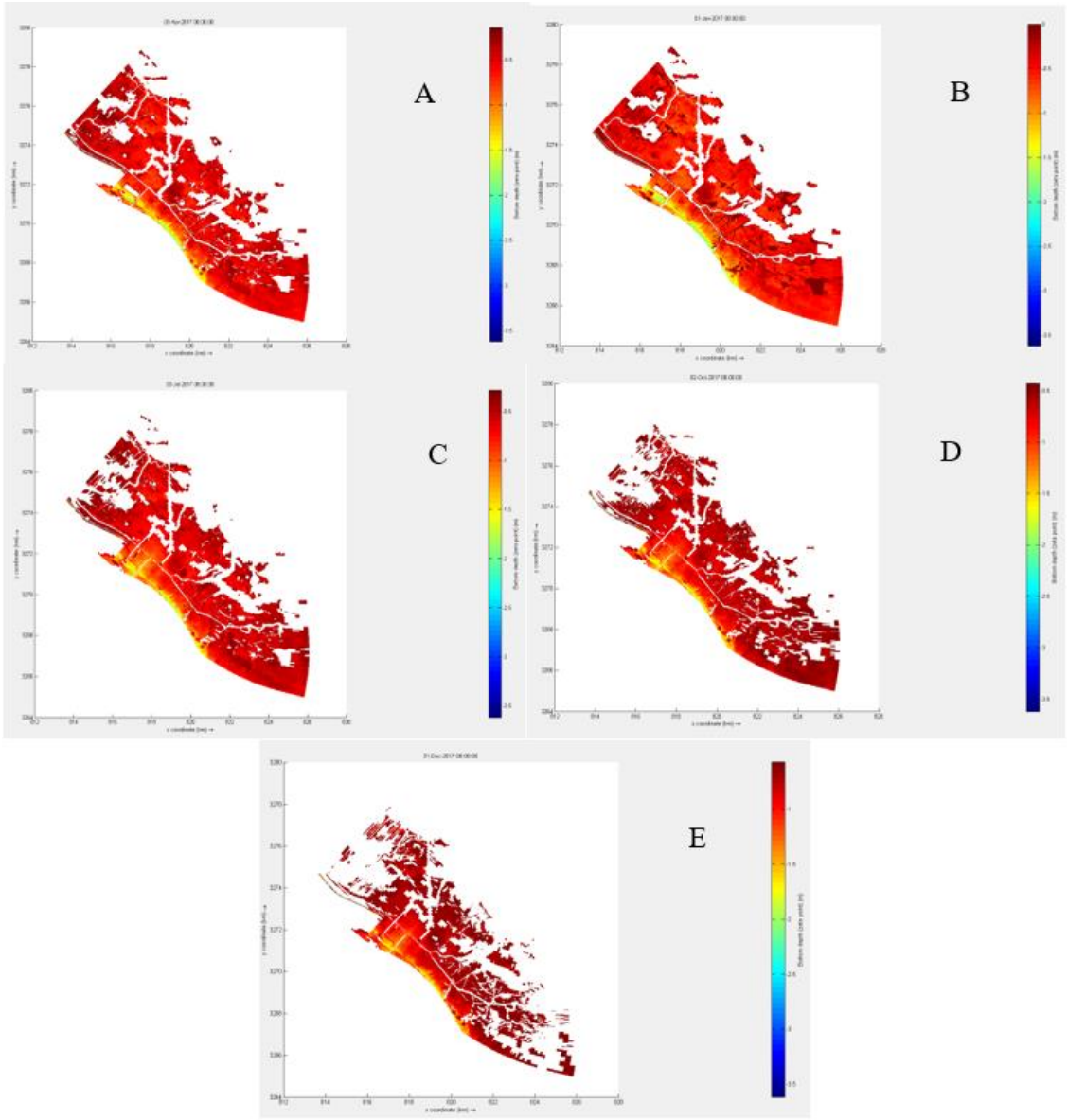

Figure 23.
(A) The beginning of the simulation with water level = 0 m. (B) After 5 years, where the water level is 0.144 m. (C) After 10 years; the water level is 0.287 m. (D) After 15 years; the water level is 0.287 m. (E) The very end of the 20-year forecast, the water level is +0.57 m.

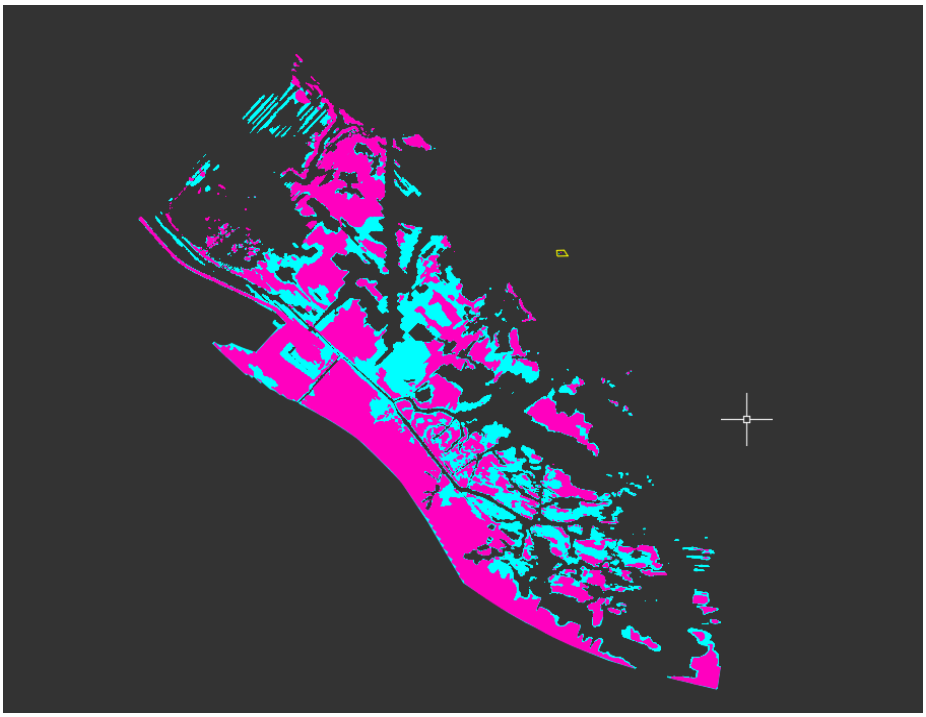

Figure 24.
The land area above +0.57 m. (Magenta) Beginning of simulation:165.296 acres. (Blue) End of 20-year simulation: 788.898 acres.

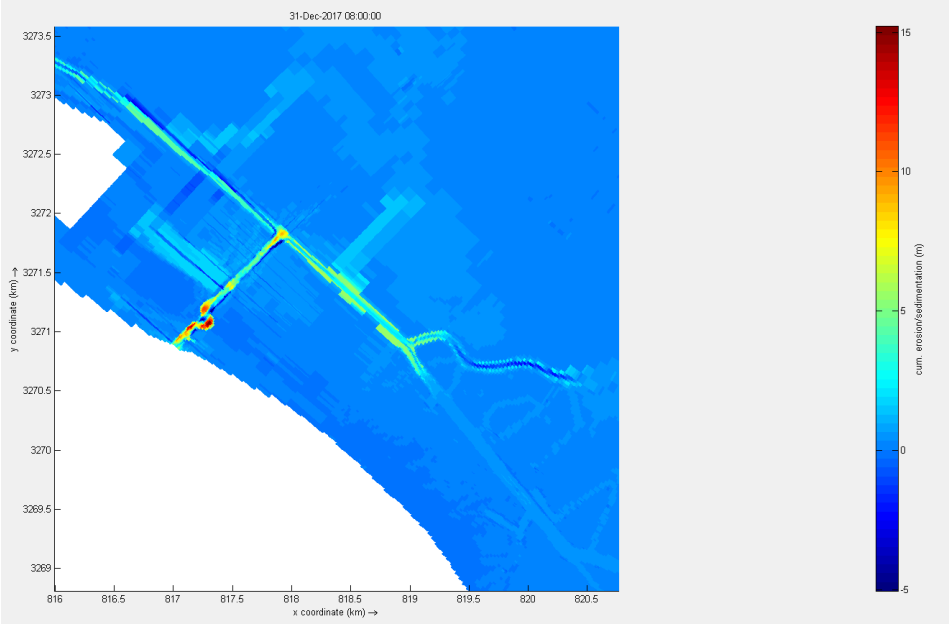

Figure 25.
Cumulative erosion and sedimentation around MGP by simulation's end. Positive values indicate deposition. Negative values indicate erosion.

Hydrodynamics

The large breach that developed on the northern bank of MGP occurred near April 12th. The volume of water flowing over the northern bank was 147% greater than the volume observed flowing over the southern bank. Before April 12, the average instantaneous overland discharge to the North from MGP was 0.56 $m^3 s^{-1}$. After the breach, the average instantaneous discharge rose to 53.9 $m^3 s^{-1}$, which caused the combined average instantaneous discharge flowing to the North to rise from 64 $m^3 s^{-1}$ to 104.3 $m^3 s^{-1}$ (Figure 26).

Interestingly, water flowing to the South rose from 98.4 $m^3 s^{-1}$ to 105.5 $m^3 s^{-1}$ (Figure 26). Before this breach established a connection to Clam Bay, the unnamed waterway experienced water flowing inland from open water 79% of the time. The average discharge was 14.9 $m^3 s^{-1}$. Following the breach, the flow was completely reversed, with water flowing inland 34% of the time. The average instantaneous discharge became 12.4 $m^3 s^{-1}$ in the opposite direction.

On average, John Bayou captured on average 47% of the flow through the junction, while Fucich Bayou captured 45%. Thus, maintaining the existing, roughly equal distribution of flow (Figure 26).

Discharge through MGP was consistently lower than what was observed in the 1-year hindcast as seen in Table 7. Deviation from the 1-year hindcast began in April.

MGP END		
Month	20 year	1 year
	Average Instantaneous Dishcarge (m^3/s)	Average Instantaneous Dishcarge (m^3/s)
Jan	116.66	116.66
Feb	130.75	130.76
Mar	187.78	188.64
Apr	284.94	320.77
May	234.69	354.42
Jun	233.02	337.71
Jul	186.50	244.87
Aug	139.66	176.72
Sep	121.06	154.75
Oct	95.35	132.76
Nov	110.11	155.71
Dec	70.50	91.02

Table 7.

Comparison of the monthly average discharge rates through the end of Mardi Gras Pass observed in the 1-year and 20-year simulations. The two simulations deviated from one another in April.

A statistical analysis comparing the average and extreme water levels observed at the end of MGP, the tidal boundary, and the MR 2017 stage record was compiled (Table 8). The highest water level observed at the end of MGP, 2.44 m, occurred on June 21. This was beyond 3 standard deviations from the average. The concurrent Cow Bayou tide level and MR stage had 5-sigma and 2-sigma deviations beyond their respective means. The lowest water level at the end of MGP, -0.074 m, occurred on January 18. A 3rd order deviation below the mean. The tide level and river stage during that time had 3rd and 2nd order deviations below their respective means.

Select Water Level Statistics: 20-year Forecast			
	MGP End	Tide Level	River Stage
Max (m)	2.44	2.41	2.24
Max Sigma	+3σ	+5σ	+2σ
Average (m)	1.04	0.71	0.95
Min (m)	-0.074	-0.502	0.064
Min Sigma	-3σ	-3σ	-2σ

Table 8.
Select water level statistics from the 20-year forecast. The river stage reflects the 2017 stage height record. The max and min sigma refers to the number of standard deviations away from the mean each max and min value is.

Hurricane Nate's impact, coupled with morphological acceleration, can be viewed as a reoccurring annual hurricane in this simulation. On October 8th, the storm surge drove the water level at the end of MGP to 2.41 m. River stage was only 0.61 m, while Cow Bayou was 2.4 m. The flow was reversed in MGP for 48 minutes on that day.

Beyond the influence of the hurricane's input, the impact of sea-level rise on the frequency of which tide levels at Cow Bayou are higher than the MR stage is significant. In Table 9, the number of occurrences can be seen to increase throughout the year, peaking in September, October, and November. In several episodes that took place on May 5, June 21, October 7, and December 7, the flow was reversed within the BLC south of MGP for a total of 45 hours and 36 minutes. Furthermore, for a sum of 1 day, 22 hours and 36 minutes, flow was reversed in the northern segment of the BLC during falling tides in January and February.

Water levels at the end of MGP and the BLC-JB junction closely resembled Cow Bayou's water levels from the beginning of the simulation up until April (Figure 27). High river stage decoupled these trends. It is not until July that the river stage decreased and the water levels at BLC-JB junction recoupled with Cow Bayou. The observation point at end of MGP became land as the mouth bar developed, splitting the BLC, and limited water level observations to high water events (Figure 22).

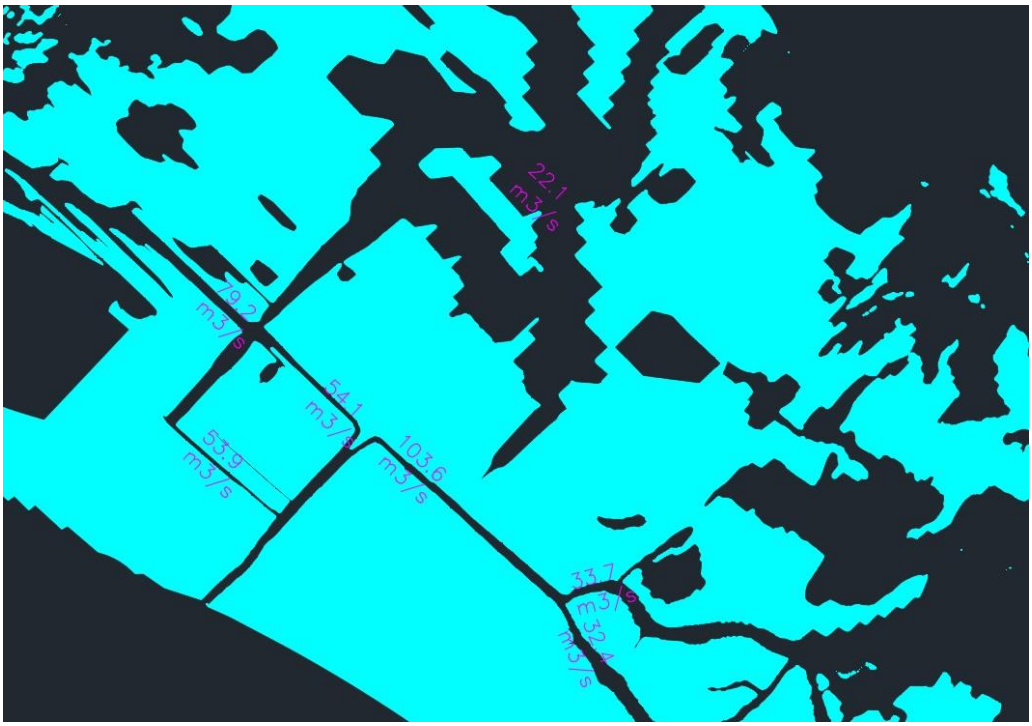

Figure 26.
Average flow distribution throughout the 20-year simulation.

Frequency of Tide At Cow Bayou Surpassing Water Levels at the Top of MGP (20-Year) & West Pointe A La Hache (1-Year)				
Month	20-Year Forecast		1-year Hindcast	
	Total Days	Percent of Month	Total Days	Percent of Month
Jan	17.2	56%	1.2	0.3%
Feb	15.2	54%	0.1	0.0%
Mar	23.7	77%	3.8	1.0%
Apr	26.8	89%	0.0	0.0%
May	28.2	91%	0.3	0.1%
Jun	29.8	99%	0.1	0.0%
Jul	29.2	94%	0.0	0.0%
Aug	30.3	98%	1.1	0.3%
Sep	29.2	97%	6.8	1.9%
Oct	31.0	100%	19.8	5.5%
Nov	30.0	100%	13.3	3.7%
Dec	29.4	97%	14.9	4.1%
Total	**320.1**	**88%**	**61.3**	**17.1%**

Table 9.
This table demonstrates the frequency with which the tide at Cow Bayou surpassed the stage height of the Mississippi River at West Pointe A La Hache during the 1-year hindcast and 20-year forecast. As sea-level rise increased during the 20-year forecast, the simulated tide at Cow Bayou is compared to the beginning of MGP.

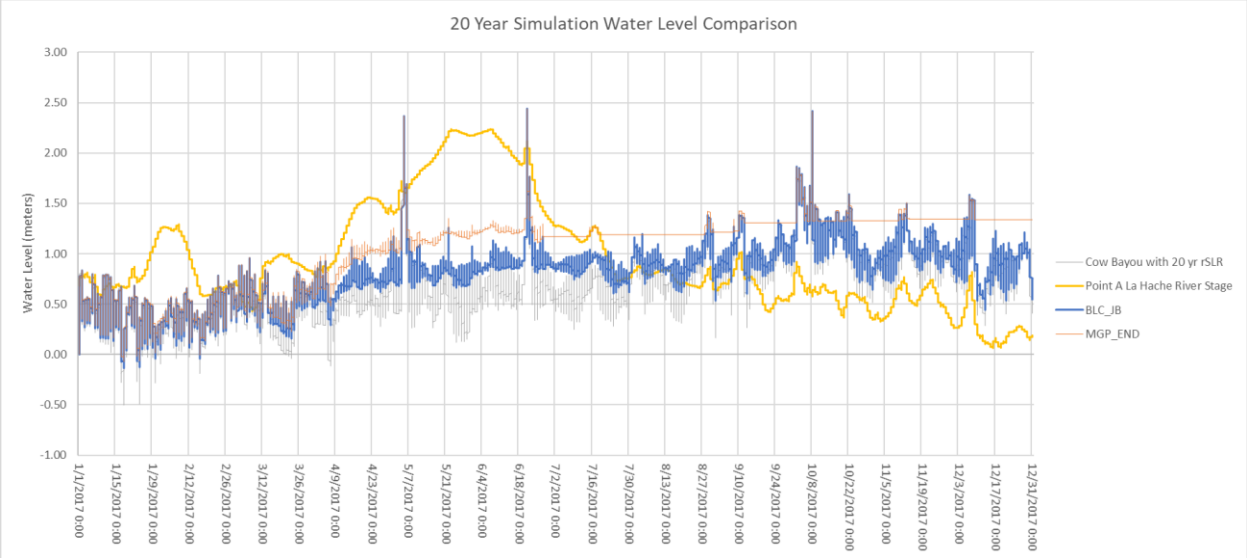

Figure 27.
Comparison of water levels throughout the 20-year simulation. Note that the location of where the observation point at the end of MGP lies became land in June.

Sediment Transport

Of the approximately 282.8 thousand-tonnes of sediment that entered MGP throughout the forecast, 95% left the channel. Of the total budget, 74% passed through the end of MGP, while approximately 21% exited laterally. By fraction, 59% and 78% of the total sand and mud were transported through the end of the channel. The approximate annual average of instantaneous suspended sediment transport exiting MGP to the North was 29%, and 68% to the South. Of the 68% of sediment transported south, only 63% reached the junction of JB and FB, which experienced a split of 45% and 42%, respectively

Examining how much of the total incoming MR sediment budget was passed through cross-sections at all outflowing boundaries of the floodplain showed that approximately 52% of the total budget exited the floodplain. The most significant conveyance was seen at the northern extent of BLC by Lower Grand Bayou, accounting for 28% of the total budget exiting the system. For reasons described earlier, this result is likely higher than what can be expected. John Bayou and Fucich Bayou passed about 10% and 4% of the total sediment budget, respectively. Clam Bay, which may not be an exit, but as a focal point for many waterways exiting the system adjacent to MGP, passed 9% of the total sediment budget out of the floodplain.

The monthly averages derived from instantaneous sand and mud volumetric sediment transport ($m^3 s^{-1}$) were calculated at the beginning, 3rd quarter mark, and end of MGP. Model results at the 3rd quarter mark and end of MGP were compared to the beginning of MGP (Tables 10 & 11). For both the 1-year hindcast and 20-year forecast, the monthly averages of sand discharge experienced the most variance. During the 1-year hindcast, monthly averaged sand transport through the end of MGP exceeded 10% of the incoming MR sand discharge from March through July and November. However, in the 20-year forecast, monthly averaged sand transport through the end of MGP surpassed 10% from March through December. The average percent of incoming MR sand discharge reaching the end of MGP throughout the forecast was 54%, and the maximum was 97%.

Occasionally, the volumetric sand transport through the end of MGP was greater than the volume passed through the 3rd quarter mark or even the end of MGP, indicating net erosion taking place within the channel between those two channel segments. During the 1-year simulation, increases in sand transport within that final segment only took place between March through August and in November (Table 10).

The 20-year forecast produced very different trends. Sand transport at the 3rd quarter mark of MGP exceeded the volumes recorded at the beginning of MGP during April and November, indicating net erosion taking place further upstream than what was seen in the 1-year hindcast. Between the 3rd quarter mark and the end of MGP, net deposition took place for all months except for February and December (Table 11).

To summarize, during the 1-year hindcast, net erosion took place more often in the downstream reach of MGP, and during the 20-year forecast, net deposition increased as flow approached the end of MGP.

Monthly averaged cohesive discharge was mostly stable during the 1-year hindcast but varied more during the 20-year forecast. During the 1-year hindcast, at least 95% of the incoming cohesive sediment was transported through the 3rd quarter mark each month except for October, where only 92% was transported. From the 3rd quarter mark to the end of MGP, most (>90%) of the cohesive sediment was transported each month, except for October (87%).

During the 20-year forecast, most of the cohesive sediment volume was transported through MGP from January through March. However, beginning in April, monthly averages ranged from 71% to 96% through the 3rd quarter mark and 64% to 88% through the last channel segment.

In both runs, January and March saw almost 100% transport of cohesive sediment through MGP. The 1-year hindcast showed that MPG transported almost 100% of the incoming cohesive sediment it received. However, during the 20-year forecast, MGP's ability to transport cohesive sediment began to diminish in April; around the same time a breach materialized on the northern bank of MGP (Table 12).

1 Year Hindcast: Monthly Suspended Sediment Trends Within MGP					
Monthly Average Instantaneous Suspended Sand Transport (m^3/s)				% of Before Bend Discharge	
Month	Before Bend	3/4 MGP	MGP End	3/4 MGP	MGP End
Jan	4.35E-05	4.13E-06	3.11E-06	9%	7%
Feb	1.93E-04	1.51E-05	1.57E-05	8%	8%
Mar	9.65E-04	1.32E-04	1.94E-04	14%	20%
Apr	2.72E-03	1.36E-03	2.29E-03	50%	84%
May	4.04E-03	2.20E-03	3.37E-03	54%	83%
Jun	3.34E-03	1.46E-03	2.22E-03	44%	66%
Jul	1.34E-03	2.73E-04	5.24E-04	20%	39%
Aug	5.11E-04	6.79E-06	7.95E-06	1%	2%
Sep	2.39E-04	3.67E-06	1.05E-06	2%	0%
Oct	1.78E-04	1.99E-06	7.57E-07	1%	0%
Nov	2.07E-04	1.13E-05	2.96E-05	5%	14%
Dec	5.58E-05	4.37E-07	1.53E-08	1%	0%
Monthly Average Instantaneous Suspended Cohesive Sediment Transport (m^3/s)				% of Before Bend Discharge	
Month	Before Bend	3/4 MGP	MGP End	3/4 MGP	MGP End
Jan	9.69E-04	9.68E-04	9.67E-04	100%	100%
Feb	3.74E-03	3.72E-03	3.72E-03	99%	99%
Mar	1.02E-02	1.01E-02	1.01E-02	100%	100%
Apr	1.74E-02	1.73E-02	1.72E-02	100%	99%
May	2.01E-02	1.92E-02	1.88E-02	95%	94%
Jun	1.58E-02	1.50E-02	1.47E-02	95%	93%
Jul	7.86E-03	7.80E-03	7.79E-03	99%	99%
Aug	3.99E-03	3.93E-03	3.92E-03	99%	98%
Sep	2.03E-03	1.98E-03	1.96E-03	98%	97%
Oct	1.61E-03	1.48E-03	1.40E-03	92%	87%
Nov	1.45E-03	1.42E-03	1.41E-03	98%	97%
Dec	7.40E-04	7.24E-04	7.18E-04	98%	97%

Table 10.
Monthly suspended sediment trends within Mardi Gras Pass taken from the 1-year hindcast for both cohesive sediment and sand.

20 Year Forecast: Monthly Suspended Sediment Trends Within MGP					
Monthly Average Instantaneous Suspended Sand Transport (m^3/s)				% of Before Bend Discharge	
Month	Before Bend	3/4 MGP	MGP End	3/4 MGP	MGP End
Jan	5.45E-05	2.25E-06	1.76E-06	4%	3%
Feb	4.23E-04	6.18E-06	8.45E-06	1%	2%
Mar	2.57E-03	5.19E-04	3.13E-04	20%	12%
Apr	4.65E-03	4.77E-03	4.24E-03	103%	91%
May	5.17E-03	3.59E-03	3.15E-03	69%	61%
Jun	3.96E-03	2.57E-03	2.30E-03	65%	58%
Jul	1.85E-03	1.15E-03	1.04E-03	62%	56%
Aug	9.72E-04	5.74E-04	4.00E-04	59%	41%
Sep	4.86E-04	3.75E-04	3.27E-04	77%	67%
Oct	3.36E-04	1.96E-04	1.50E-04	58%	45%
Nov	4.00E-04	4.16E-04	3.86E-04	104%	97%
Dec	6.75E-05	1.04E-06	9.85E-06	2%	15%
Monthly Average Instantaneous Suspended Cohesive SedimentTransport (m^3/s)				% of Before Bend Discharge	
Month	Before Bend	3/4 MGP	MGP End	3/4 MGP	MGP End
Jan	9.69E-04	9.68E-04	9.67E-04	100%	100%
Feb	3.75E-03	3.73E-03	3.72E-03	99%	99%
Mar	1.02E-02	1.02E-02	1.01E-02	100%	99%
Apr	1.73E-02	1.67E-02	1.52E-02	96%	88%
May	1.96E-02	1.38E-02	1.25E-02	71%	64%
Jun	1.55E-02	1.10E-02	1.02E-02	71%	66%
Jul	7.83E-03	6.09E-03	5.95E-03	78%	76%
Aug	3.98E-03	3.16E-03	3.12E-03	79%	78%
Sep	2.01E-03	1.60E-03	1.54E-03	80%	77%
Oct	1.54E-03	1.16E-03	1.02E-03	75%	66%
Nov	1.38E-03	1.09E-03	1.01E-03	79%	73%
Dec	7.15E-04	5.79E-04	5.56E-04	81%	78%

Table 11.
Monthly suspended sediment trends within Mardi Gras Pass taken from the 20-year forecast for both cohesive sediment and sand.

Month	MGP END (m3/s)	NoMGP Overland (m3/s)
Jan	9.67E-04	1.67E-10
Feb	3.72E-03	1.46E-10
Mar	1.01E-02	1.38E-05
Apr	1.52E-02	3.25E-04
May	1.25E-02	1.55E-03
Jun	1.02E-02	2.05E-03
Jul	5.95E-03	2.00E-03
Aug	3.12E-03	1.85E-03
Sep	1.54E-03	1.69E-03
Oct	1.02E-03	1.56E-03
Nov	1.01E-03	1.45E-03
Dec	5.56E-04	1.35E-03

Table 12.

Monthly average of suspended cohesive sediment transport through the end of Mardi Gras Pass, and the northern bank of Mardi Gras Pass throughout the 20-year forecast. The northern bank eventually develops a breach around April 12th, which grows throughout the year. As this breach grows, it captures more of the suspended sediment transport from the end of Mardi Gras Pass.

Discussion

The combination of efficient arteries of sediment delivery to distal basins, and tidal modulation, ensured the extensive delivery of relatively higher concentrations of suspended sediment carried by floodwaters throughout the floodplain (Figure 28). Tidal modulation facilitated through the channelized waterways made these channels efficient at delivering sediment several kilometers away from the MR due to their ability to maintain high levels of kinetic energy throughout the receiving basin. The interaction between fluvial input and tidal modulation within these channels governed sediment transport throughout the floodplain. Falling tides accelerated flow out to sea. For instance, even at low MR flows through MGP, the ebbing tide currents, when compared to flood tides, accelerated flow through these channels, and transported sediment for longer distances. However, the incoming tide opposed the fluvial, seaward directed currents, creating a backwater effect.

The decelerated currents provided opportunities for sediment deposition, while the increase in water level within the waterways due to the backwater effect reached overbank elevations and eventually flooded the surrounding marsh platform. In the absence of tidal and subtidal forcing, the simulated water levels never flooded the marsh platform even during high water from the MR. The existing network of channels appeared to transport water and sediment beyond the floodplain effectively. Without domain-wide overbank flooding to deliver mineral sediment onto the marsh platform, the marsh can only vertically aggrade via flooding caused by storms and through organic accumulation. This is evident when comparing the amount of sediment retained within the domain in each simulation. Tidal and subtidal water level excursions increased the amount of sediment retained by at least 11% (Table 6).

The correlation between suspended sediment transport and the MR's stage demonstrated that during floods, the high-pressure gradient from the river to the receiving basin increased flow and bed shear stresses. The May - June flood event was the year's peak discharge event. Despite the tide imparting a 7% to 8% hindrance on discharge through the end of MGP during that event, suspended sediment transport remained above average. However, tide levels at Cow Bayou were above the river stage for approximately 17% of the hindcast. This phenomenon occurred most frequently in the second half of the year when the river stage was low, and the hurricane season was active (Table 9). During this season, flow velocity through MGP was greatly diminished due to a low water level gradient from the river to the basin. This impedance of flow velocity forced most incoming MR suspended sand to deposit within MGP (Table 10). Hence, the Mississippi River is the dominant force of morphologic change within MGP. However, forecast results predicted that the effects of SLR would likely alter this behavior.

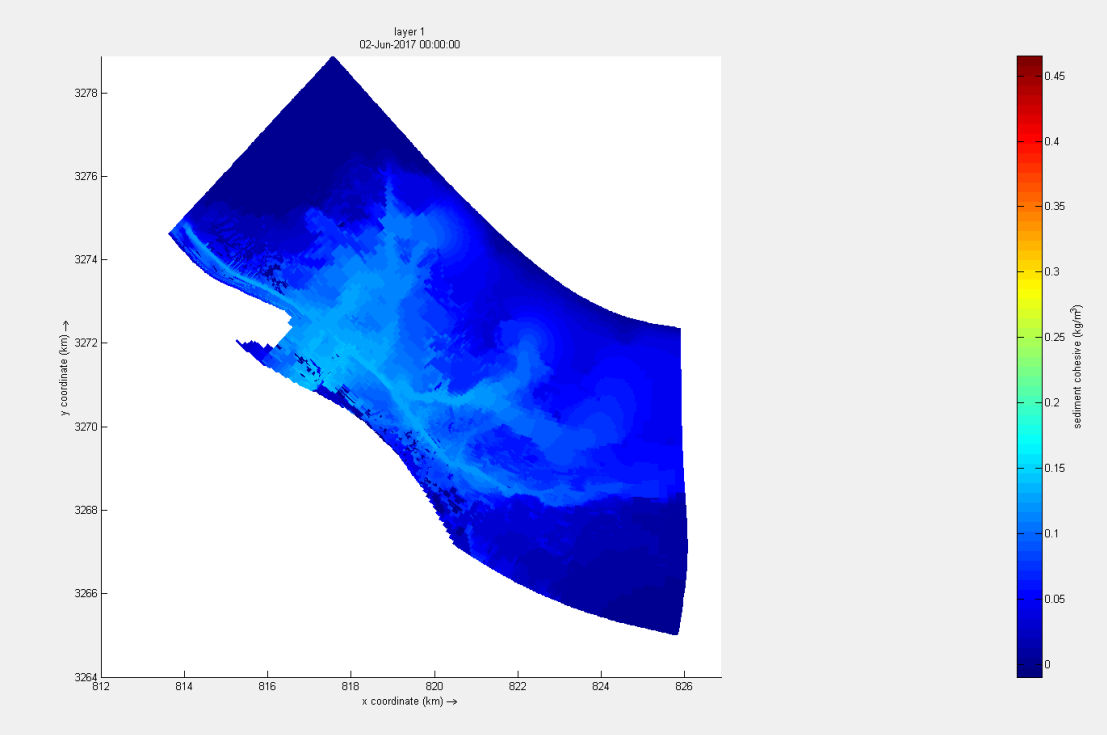

Figure 28.
Distribution of suspended cohesive sediment concentration throughout the domain during the May-June flood event with falling tide.

During late March and early April of the 20-year forecast, suspended sand transport increased relative to the hindcast through the end of MGP. However, suspended cohesive sediment transport rates began to decline (Table 11). The explanation for this phenomenon is likely the result of a combination of several factors.

The monthly averages of instantaneous suspended sand transport through MGP increased significantly in the months following March (Table 11). This increase coincided with the straightening of MGP during the latter half of March. The straightening of the channel and the subsequent elevated suspended sand transport observed at the end of MGP were likely due to the tremendous morphological acceleration used to simulate 20 years of morphological processes. This method of morphological acceleration assumed that the simulated year occurred as is for the remaining 19 years. The straightening of MGP's upper reach transported a considerable amount of sediment further down its channel and into the BLC. The bank erosion, in addition to the MR sediment load, was deposited along the bottom and banks of MGP's receiving channels as the flow lost energy. This influx of sediment and subsequent deposition caused the BLC to become narrower and shallower for the entirety of the southern branch toward its junction with JB, and for approximately 3100 m along the northern branch.

The declining suspended cohesive sediment transport after April could be explained partially by the development of several breaches along the northern bank of MGP, which created several exit points for flow and sediment to escape laterally before the lower end of the channel. The largest of these breaches formed in April.

Sea-level rise imposed linearly over the forecasted period gradually inundated the basin; this process slowly forced the tide at Cow Bayou to be higher than water levels at the beginning of MGP. The tide at Cow Bayou was higher for approximately 88% of the 20-year forecast (Table 9). This was a significant increase compared to 2017, where it only occurred approximately 17% of the year. In addition, the frequency with which water levels were above 1 m at the end of MGP increased, totaling about 257 days, or in other words, 71% of the year. At this elevation, much of the floodplain became inundated, even after 20-years of simulated vertical aggradation. Under these conditions, approximately 95% of the cumulative total sediment passed through the first upstream cross-section in MGP left the channel. Of that, the floodplain retained approximately 44%, with the remaining sediment exiting into the open sea.

In reality, sea-level rise signals would be widespread. They are anticipated to affect the modern delta and, ultimately, the Mississippi River itself, suggesting that the river stage would gradually increase with sea-level rise (Passeri, Hagen, Medeiros, Bilskie, Alizad, & Wang, 2015). This makes the model results less conservative, as the river would strive to maintain a similar head differential with the receiving basin, all other influences aside. However, with increasing inundation, comes an increase in accommodation that will need to be filled. This experiment can serve as a first-order look at the initiation of submergence.

While much of the floodplain was able to aggrade vertically by utilizing the incoming MR sediment load, a net loss of land was observed in Figure 29, with much of the loss occurring along the outer fringes of the floodplain that received less of the MR sediment. Along the periphery of the marsh, suspended sediment transport was greatly diminished. Without an adequate sediment supply to support deposition, headward erosion along the margins of the floodplain transpired as the tide withdrew, scouring new drainage paths. The sediment that was retained in the floodplain contributed to allowing approximately 624 acres to aggrade above +0.57 m in elevation vertically. An estimated 382 acres of land was transformed into open water (Figure 29). For areas with an existing network of canals and bayous such as Southeastern Louisiana, the installation and operation of sediment diversions are likely to experience results similar to this study, and thus benefit from the widespread delivery of relatively higher SSC as the receiving basin is gradually lowered due to sea-level rise.

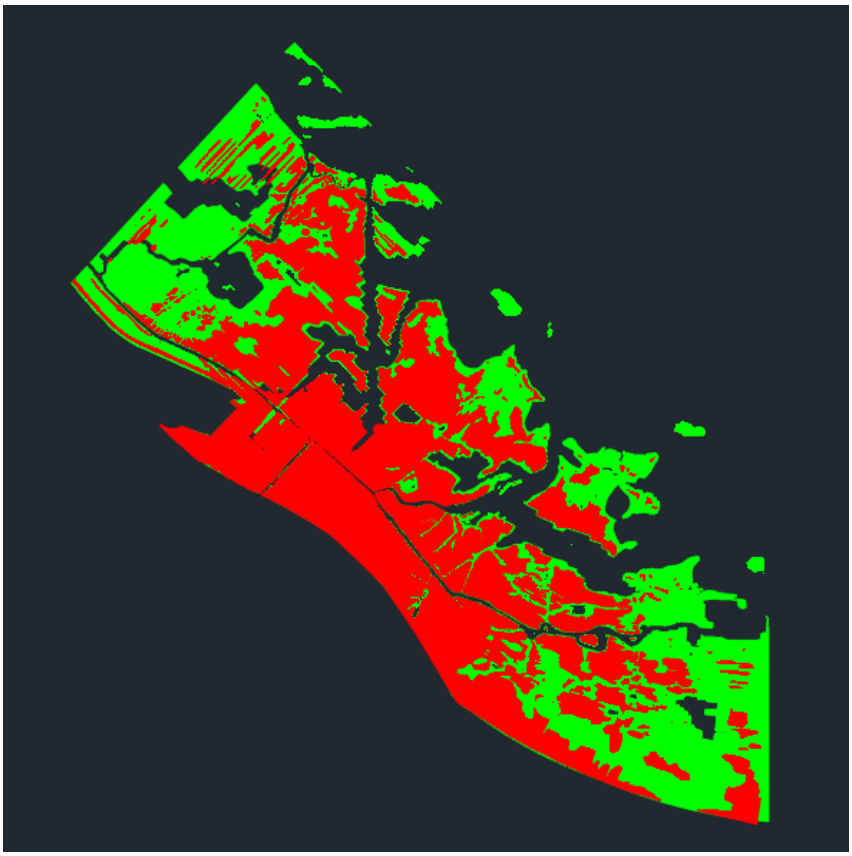

Figure 29.
(Green) Starting land area (water level = 0 m) compared to (Red) after 20 years of simulated morphological change (water level = +0.57 m).

With these results now in focus, it is important to discuss the limitations of Delft3D's capabilities and the simulations' approach and their implications. Some important considerations beyond the capabilities of Delft3D are its inability to take into account the myriad of complex bio-geomorphological processes within this area without a great and comprehensive effort beyond this thesis' scope. This study also forwent analyzing salinity's effect on the domain, focusing solely on the morphologic and hydrologic processes. The study domain excluded the adjacent section of the MR, and thus, the study was limited in its ability to capture any reasonable temporal and spatial variations of the MR and the MGP outlet, along with MR overbank flow. The omission of which, meant that the study neglected to examine the effects SLR might have on this reach of the MR, and the subsequent consequences for the study area. Lastly, it would be imprudent to believe that future hydrodynamic processes would perform exactly as one years' worth of simulation under such a significant acceleration.

Firstly, this numerical model did not take into consideration the effects flora and fauna may have on vertical marsh accretion and the effects of environmental stressors caused by SLR. For example, according to a synthesis of studies compiled by Jessie C. Jarvis in 2010 for the U.S. Army Engineer Research and Development Center, organic sediment accounts for 62% of vertical accretion, and vertical accretion rates in the study area can range anywhere from 0.60 ± 0.07 to 0.73± 0.13 cm yr^{-1}. If a conservative rate of vertical accretion was chosen, 0.5 cm yr^{-1}, and applied for 20 years, it can be assumed that much of the consistently subaerial floodplain that can support wetland flora would be 10 cm higher than what was observed. The root systems of wetland plants can act as an erosion-resistant turf, impeding the rates of erosion along channel banks and throughout the floodplain (Hardaway & Gunn, 2009). While the numerical model employs Chezy roughness coefficients and critical bed shear stress for erosion rates that attempt to simulate the effects vegetation has on impeding erosion, it most likely does not comprehensively simulate the varying spatial and temporal reality one could expect at the study area.

One must also consider the stress SLR can impart upon the domain. Salinity intrusion and excessive waterlogging are stressors that hinder the plants' ability to aid in sediment accretion (Jarvis, 2010). As SLR outpaces the floodplain's ability to accrete vertically, these environmental stressors will reduce plant production and will eventually lead to death (Webb et al. 1995). Once large communities of plants die off, their root systems collapse, accelerating subsidence, where they once lived (DeLaune et al., 1994). In turn, this has a positive feedback effect on plant communities further inland, sustaining the pattern of degradation (DeLaune et al., 1994).

Lastly, as sea-level rise continues, stage height along the river's lower reach will increase to address the shifting water slope at the interface of the river and the sea. Due to the difficulty of creating a domain that included a section of the Mississippi River and the entrance of MGP, a simple, static inflow boundary with a forced discharge was used. The inflow boundary at MGP only accounted for discharge, and not any changes in water level or slope. Hence, it was impossible to replicate the expansion of the entrance of MGP with the boundary condition chosen. The expansion would have increased discharge through MGP, similar to what has been observed historically. Furthermore, MGP's entrance will likely meander over time. In short, this experiment did not model the effects rising stage height would have on the Bohemia Spillway region.

The forecast results were used to provide input to Equation 1 from Nienhuis et al. (2018) and compared to their findings. The floodplain erosion rate (E) was much larger than the floodplain deposition rate (D). According to Nienhuis et al. (2018), this indicates a potential avulsion or the onset of an avulsion, at least, as the initial erosion exceeds distal aggradation. This result is antithetical to what was observed from the simulation. Rather, the forecast results were more in line with what their study found when crevasse splays formed. The upper reach of the breach channel eroded. The associated increase in sediment supply caused deposition across the floodplain, which decreased the local water surface slope at the breach. During this phase, new land was rapidly formed and infilling of the levee breach with bedload sediments occurred. Nienhuis et al. (2018) utilized a schematized basin without an existing network of channels; therefore, Equation 1 may not be appropriate for floodplains with an existing channel network.

Conclusion

The results from comparing the 1-year hindcast to the 1-year simulation without tidal or subtidal forces demonstrated that, currently, Mardi Gras Pass is river-dominated. The river's stage height is the primary force determining deposition and erosion within Mardi Gras Pass. The existing network of channels efficiently carried the sediment supplied from the Mississippi River across the domain. However, the vertical aggradation of the surrounding floodplain depended on tide-induced inundation. Without tidal and subtidal forces, vertical aggradation of the floodplain would not occur.

During the 20-year forecast, flood-induced bank erosion released a considerable volume of sediment. A backwater effect created by the rising tides encouraged the deposition of the newly released bank sands within the proximal and distal waterways, reducing the depths and widths of Mardi Grass Pass and the Back Levee Canal. The released sand also contributed to the development of a mouth bar at the end of Mardi Gras Pass, bisecting the Back Levee Canal. The development of the mouth bar hampered flow to the North considerably. This combination of sea-level rise, tidal modulation, and channel infilling promoted floodplain reorganization, prompting the development of several breaches within Mardi Gras Pass. The largest of these breaches developed on its northern bank and persisted throughout the forecast. This breach could be the beginning of a minor avulsion, changing the course of Mardi Gras Pass.

Tides continued to be an important process through which they contributed to marsh sedimentation by modulating backwater flows and aiding in overbanking and sediment deposition on the marsh platform. By the end of the forecast, 624 acres of marsh underwent vertical mineral aggradation beyond the estimated 20-year mean sea level of +0.57 m. However, because of the pace of sea-level rise, 382 acres of marsh were converted into open water. The ability of tides to modulate channel currents and thus continue to promote marsh platform sedimentation will gradually diminish over time. The rate at which marsh platforms will aggrade will eventually become outstripped by the rate of sea-level rise and eventually lead to submergence unless sufficient organic production is present to offset the deficit.

Bibliography

ASTM. (1997). Standard test methods for determining sediment concentration in water samples. ASTM D 3977-97.

Bagnold, R. A. (1966). An approach to the sediment transport problem. *General Physics Geological Survey, Prof*. paper.

Bolla Pittaluga, M., Repetto, R., & Tubino, M. (2003). Channel bifurcation in braided rivers: Equilibrium configurations and stability. Water Resources Research, 39(3), 1046. https://doi.org/10.1029/2001WR001112

Boyd, E., Baker D., Henkel, T., Hillmann, E., Lopez, J., Moshogianis, A., 2012. Summary of Observed Depths and Widths Mardi Gras Pass in the Bohemia Spillway, Southeast Louisiana: August 2012 Update.

Chamberlain, E. L. (2018). Delta Dynamics. (cover story). *Natural History*, 126(6), 24. Retrieved From http://ezproxy.uno.edu/login?url=http://search.ebscohost.com/login.Aspx?direct=true&db=f6h&AN=129708000&site=eds-live&scope=site

Cretini, F., Lopez, J., Henkel, T., Hillmann, E., Smith, P., Baker D., Butcher, K., 2016. Summary of Observed Channel Dimensions in Mardi Gras Pass in the Bohemia Spillway, Southeast Louisiana: November 14 & 15, 2016. Lake Pontchartrain Basin Foundation.

Coastal Protection and Restoration Authority (2017). Louisiana's comprehensive master plan for a sustainable coast. Baton Rouge, LA: Coastal Protection and Restoration Authority of Louisiana.

Danielson, J. J., Poppenga, S. K., Brock J. C., Evans, G. A., Tyler, D. J., Gesch, D. B., Thatcher, C. A., and Barras, J. A. (2016). Topobathymetric elevation model development using a new methodology: coastal national elevation database, *Journal of Coastal Research,* 76(sp1), 75-89. https://doi.org/10.2112/SI76-008

Deltares (2014). Delft3D Flow User Manual version 3.15.34158. Delft, Netherlands: Deltares. Retrieved from www.delftsoftware.com

Deltares (2015) Delft3D; Simulation of Multi-Dimensional Hydrodynamic Flows and Transport Phenomena, Including Sediments, Hydro-Morphodynamics; Deltares: Delft, The Netherlands.

Edmonds, D. A., & Slingerland, R. L. (2007). Mechanics of river mouth bar formation: Implications for the morphodynamics of delta distributary networks. *Journal of Geophysical Research: Earth Surface, 112*(F2).

Esposito, C. R., Shen, Z., Törnqvist, T. E., Marshak, J., & White, C. (2017). Efficient retention of mud drives land building on the Mississippi Delta plain. Earth Surface Dynamics, 5(3), 387–397. https://doi.org/10.5194/esurf-5-387-2017

Fisk, H. N. (1952). Geological investigations of the Atchafalaya Basin and problem of Mississippi River diversion. Vicksburg, MS: US Army Corps of Engineers.

Gagliano, S. M., & Van Beek, J. L. (1975). An approach to multiuse management in the Mississippi Delta System. In M. L. Broussard (Ed.), Deltas: Models for exploration
(pp. 223–238). Houston, TX: Houston Geological Society.

Georgiou, I.Y., Yocum, T. (2018). Measurements of lateral flow from the Mississippi River at Mardi Gras Pass and flow distribution within the Bohemia Spillway using synoptic and tripod ADCP observations. A technical report submitted to the Lake Pontchartrain Basin Foundation (LPBF), Pontchartrain Institute for Environmental Sciences (PIES), University of New Orleans, New Orleans LA. 70pp.

Hajek, E. A., & Edmonds, D. A. (2014). Is river avulsion style controlled by floodplain morphodynamics? Geology, 42(3), 199–202. https://doi.org/10.1130/G35045.1

Hardaway, S.C., & Gunn, J.R. (2010). Design and performance of headland bays in Chesapeake Bay, USA. Coastal Engineering, 57(2), 203-212.

Henkel, T., Lopez, J., Hopkins, M., Butcher, K., Hillmann E., and Songy, A. (2018). Mardi Gras Pass regional influence: Sediment distribution and deposition, salinity and nutrients in 2017. Lake Pontchartrain Basin Foundation. 31pp.

Ikeda, S. (1982). Incipient motion of sand particles on side slopes. *Journal of the Hydraulics Division, 108*(1), 95-114.

Kleinhans, M. G., Jagers, H. R. A., Mosselman, E., & Sloff, C. J. (2008). Bifurcation dynamics and avulsion duration in meandering rivers by 1-dimensional and three-dimensional models. Water Resources Research, 44, W08454. https://doi.org/10.1029/2007WR005912

Lesser, M. P., Weis, V. M., Patterson, M. R., & Jokiel, P. L. (1994). Effects of morphology and water motion on carbon delivery and productivity in the reef coral, Pocillopora damicornis (Linnaeus): diffusion barriers, inorganic carbon limitation, and biochemical plasticity. *Journal of Experimental Marine Biology and Ecology, 178*(2), 153-179.

Lopez, J., Henkel, T., Boyd, E., Conner, P., Milliken, M., Baker, A., Martinez, L. (2013). Bohemia Spillway in Southeastern Louisiana: History, General Description, and 2011 Hydrologic Surveys. Lake Pontchartrain Basin Foundation. 178pp.

Mohrig, D., Heller, P. L., Paola, C., & Lyons, W. J. (2000). Interpreting avulsion process from ancient alluvial sequences: Guadalupe-Matarranya system (northern Spain) and Wasatch Formation (western Colorado). Geological Society of America Bulletin, 112(12), 1787. https://doi.org/10.1130/0016-7606(2000)112%3C1787:IAPFAA%3E2.0.CO;2

Nardin, W., & Edmonds, D. A. (2014). Optimum vegetation height and density for inorganic sedimentation in deltaic marshes. Nature Geoscience, 7(10), 722–726. https://doi.org/10.1038/ngeo2233

Nienhuis, J. H., Törnqvist, T. E., & Esposito, C. R. (2018). Crevasse splays versus avulsions: A recipe for land building with levee breaches. Geophysical Research Letters, 45, 4058–4067. https://doi.org/10.1029/ 2018GL077933

Parker, G., Toro-Escobar, C. M., Ramey, M., & Beck, S. (2003). Effect of floodwater extraction on mountain stream morphology. *Journal of Hydraulic Engineering, 129*(11), 885-895.

Partheniades, E. (1965). Erosion and deposition of cohesive soils. *Journal of the Hydraulics Division, 91*(1), 105-139.

Passeri, D.L., Hagen, S.C., Medeiros, S.C., Bilskie, M.V., Alizad, K. and Wang, D. (2015), The dynamic effects of sea level rise on low-gradient coastal landscapes: A review. Earth's Future, 3: 159-181. doi:10.1002/2015EF000298

Rajiv Sinha. (2009). The Great avulsion of Kosi on 18 August 2008. *Current Science*, (3), 429. Retrieved from http://ezproxy.uno.edu/login?url=http://search.ebscohost.com/login.aspx?direct=true&db=edsjsr&AN=edsjsr.24112012&site=eds-live&scope=site

Schumm, S., & Lichty, R. (1963). Channel widening and flood-plain construction along Cimarron River in southwestern Kansas. Geological Survey Professional Paper, 352(D), 71–88.

Shaw, J. B., Mohrig, D., & Whitman, S. K. (2013). The morphology and evolution of channels on the Wax Lake Delta, Louisiana, USA. *Journal of Geophysical Research: Earth Surface, 118*(3), 1562-1584.

Slingerland, R., & Smith, N. D. (1998). Necessary conditions for a meandering-river avulsion. Geology, 26(5), 435–438. https://doi.org/10.1130/0091-7613(1998)026%3C0435:NCFAMR%3E2.3.CO;2

Smith, N. D., Cross, T. A., Dufficy, J. P., & Clough, S. R. (1989). Anatomy of an avulsion. Sedimentology, 36(1), 1–23. https://doi.org/10.1111/j.1365-3091.1989.tb00817.x

Songy, A., Hopkins, M., Lopez, J., Henkel, T., Hillmann, E., Baker, D., & Butcher, K., (2018). Summary of Observed Channel Dimensions in Mardi Gras Pass in the Bohemia Spillway, Southeast Louisiana: November 2017 Update. Lake Pontchartrain Basin Foundation. 22pp.

Sweet, W.V., Kopp, R. E., Weaver, C. P., Obeysekera, J., Horton, R., Thieler, E. R., & Zervas, C. (2017). *Global and regional sea level rise scenarios for The United States* (NOAA Technical Report NOS CO-OPS 083).

Van Rijn, L. C. (1993). *Principles of sediment transport in rivers, estuaries and coastal seas* (Vol. 1006). Amsterdam: Aqua publications.

Yocum, T., & Georgiou, I. (2016). Growth laws for sub-delta crevasses in the Mississippi River Delta: Observations and Modeling (Published doctoral prospectus). University of New Orleans, New Orleans, USA.

Appendices

Appendix A. Overview of Delft3D input parameters.

Param	Value	Units	Description
General			
Tstart	0	min	Start time
Tstop	524172	min	Stop time (maximum)
Dt	0.4	min	Timestep
Ag	9.81	ms^{-2}	Gravitational Acceleration
Flow			
Rhow	1000	kgm^{-3}	Water Density
Salw	0	ppt	Salinity
Rhoa	1	kgm^{-3}	Air Density
Ccofu	35	$m^{0.5}s^{-1}$	Chezy roughness u
Ccofv	35	$m^{0.5}s^{-1}$	Chezy roughness v
Vicouv	1		Uniform horizontal eddy viscosity
Dicouv	10		Uniform vertical eddy diffusivity
slip condition	free		Wall roughness
Dryflc	0.1	m	Threshold depth for drying and flooding
Tlfsmo	120	min	Time interval to smooth hydrodynamic boundary conditions
Rettis(1)	0	min	Inlet Thatcher Harlemann return time
Rettis(2)	0	min	Floodplain Thatcher Harlemann return time
Morphology			
EpsPar	false		Vertical mixing distribution according to van Rijn
MorFac	1 or 20		Morphological scale factor
MorStt	720	min	Spin-up interval from TStart to the start of mor. changes
Thresh	0.050000001	m	Threshold sediment thickness for transport and erosion
MorUpd	true		Update bathymetry during FLOW simulation
CMPUds	true		Update bed composition during flow run
EqmBc	false		Equilibrium sand concentration profile at inflow boundaries
DensIn	true		Include effect of sediment concentration on fluid density
Sus	1		Multiplication factor for suspended sediment ref. concentration

Vita

The author was born in Panama City, Panama. He graduated with a Bachelor of Science in Geology in 2012 from Towson University in Maryland. He joined the Earth and Environmental Science department of the University of New Orleans to pursue his master's degree and became a member of Professor Ioannis Georgiou's research group in 2017. He began working as a geoscientist in Maryland before graduation, engineering stream restorations, living shorelines, and other ecological restoration and storm water management projects. This thesis was completed while lockdowns across the US were issued in reaction to the COVID-19 pandemic.